WWB Spring Barrier in ENSO — Part I: A Theoretical Framework

Jie Hu[a], Haijun Yang*[a], and Yishuai Jin[b]

[a] *Department of Atmospheric and Oceanic Sciences and Key Laboratory of Polar Atmosphere-ocean-ice System for Weather and Climate of Ministry of Education, Fudan University, Shanghai 200438, China*

[b] *State Key Laboratory of Physical Oceanography, Ocean University of China, Qingdao 266100, China*

Journal of Climate

March 28, 2026

Submitted

**Corresponding author*: Haijun Yang, yanghj@fudan.edu.cn

ABSTRACT

Westerly Wind Bursts (WWBs) are key external disturbances in event-scale ENSO evolution, yet their timing-dependent effects lack a unified theoretical explanation. Using the recharge–discharge oscillator framework of Jin (1997), we idealize a finite-duration WWB as a pulse forcing and derive analytical solutions for the resulting ENSO response. The solutions show that WWB impacts are strongly modulated by the seasonal background growth rate associated with the Bjerknes feedback, producing a "WWB Spring Barrier" and a summer–autumn amplification window. Mechanistically, the total response decomposes into two components: a same-frequency direct response governed by the intrinsic ENSO frequency, and a seasonally modulated adjustment response delayed by several months, arising from the convolution of thermocline adjustment with the seasonal growth rate. The direct term does not exhibit a spring barrier, whereas the adjustment term shows pronounced seasonal suppression. Parameter sensitivity analyses indicate that the initial phase of the background growth rate determines the season of ENSO phase locking. In addition, WWB-induced responses over short horizons (1–3 months) are nearly independent of the intrinsic ENSO frequency. These results provide concise and testable diagnostics for identifying when WWBs are most effective and link seasonal phase locking and the spring predictability barrier to event-scale external forcing within a unified theoretical framework.

Keywords: ENSO; Westerly Wind Bursts; Spring Barrier; seasonal growth rate; analytical solution; adjustment response

1. Introduction

El Niño–Southern Oscillation (ENSO) is one of the most important interannual climate oscillations with far-reaching impacts on the global climate system (McPhaden et al. 2020). Its occurrence and evolution affect agriculture (Henson et al. 2017), ecosystems (Lehodey et al. 2020), public health (Heaney et al. 2019), and socioeconomic activities (Hsiang et al. 2011), making ENSO prediction a central topic in climate dynamics (Yang et al. 2018). Despite significant progress in extending ENSO forecast lead time using coupled numerical models, statistical approaches, and more recently, data-driven techniques (Ham et al., 2019; Hu et al., 2021; Petrova et al., 2020; Ren et al., 2018, 2019; Saha et al., 2014; Wang et al., 2020; Zebiak & Cane, 1987), ENSO prediction remains constrained by initial-condition uncertainty, nonlinear coupling, and changes in the background state (Ehsan et al. 2024; Jin et al. 2008; Santoso et al. 2019; Zhang et al. 2021; Zheng et al. 2022). The Spring Predictability Barrier (SPB) is particularly prominent: regardless of whether forecasts are initialized before or after spring, model skill typically degrades during boreal spring (April–June) (Ham et al. 2019; Hu et al. 2021; Luo et al. 2008). Observations—including tropical Pacific sea-surface temperature (SST) (McPhaden 2003; Ren et al. 2016), sea-level pressure (Webster and Yang 1992), and precipitation (Wright 1979)—likewise show a rapid decay of autocorrelation during this season. In this work, we refer to seasons by the boreal convention: winter (December–February), spring (March–May), summer (June–August), and autumn (September–November).

The SPB is an intrinsic feature produced by the annual cycle of the tropical Pacific background state, which modulates ENSO's intrinsic growth rate (Jin et al. 2019). The background state exhibits a rapid warming during spring and a rapid cooling during summer (Fig. 1a), thereby imprinting a clear seasonality on the ENSO growth rate (Moore and Kleeman 1996; Stein et al. 2010; Thompson and Battisti 2001; Webster and Yang 1992), which is quantified in Fig. 1b. During summer–autumn, the Bjerknes positive feedback is the strongest, enhancing air–sea coupling so that ENSO oscillations can be self-sustained and amplified. As winter sets in, thermodynamic damping in the surface ocean intensifies, while the efficiency of wind–SST coupling weakens; together they diminish or even offset the Bjerknes feedback, leading to a gradual decline in the system's effective gain (Jin et al. 2019; Levine and McPhaden 2015; Liu et al. 2019). During this period, ENSO's self-amplification capacity is weakest, anomalies struggle to accumulate and persist across spring, and the autocorrelation coefficient (ACC) of SST anomaly (SSTA) drops sharply when crossing boreal spring (Fig. 1c).

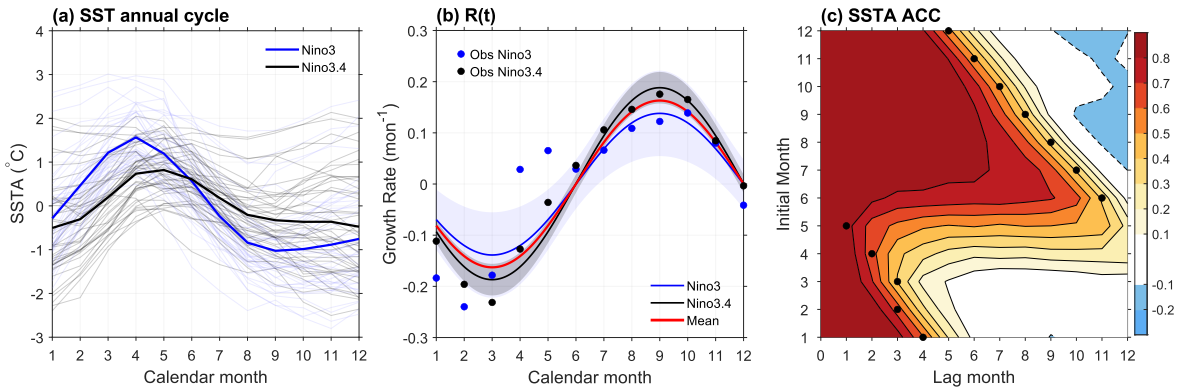

FIG. 1. Seasonal variations of the SSTA (units: °C) and the background growth rate (units: month^{-1}) in the tropical Pacific, as well as the ACC of SSTA. (a) Monthly deviations of SSTA in Niño-3 (blue) and Niño-3.4 (black) regions. Annual mean value (1982-2024) is removed. (b) Seasonal cycle of growth rate. Dots indicate the growth rates obtained from observations, following the method of Jin and Liu (2021). Curve represents a regression fit. Blue (black) is for Niño-3 (Niño-3.4) region. Red curve is for the mean of Niño-3 and Niño-3.4 region. The fitted red curve $R(t) = R_0 - R_1 \sin(\omega_1 t + \varphi)$, with $R_0 = 0.0007$ month^{-1}, $R_1 = 0.19$ month^{-1}, $\varphi = \frac{2\pi}{12}$ rad and $\omega_1 = \left(\frac{2\pi}{12}\right)$ month^{-1}. (c) Persistence map for Niño-3 SSTA during 1982–2024, illustrating the Spring Predictability Barrier (SPB). Black dots mark the lag months of maximum autocorrelation decline for different initial months. These results are based on Extended Reconstructed SST Version 6 (Huang et al. 2025). Similar results can be obtained using the Hadley Centre Global Sea Ice and SST dataset (Rayner et al. 2003) or NOAA Optimum Interpolation SST version 2 (Huang et al., 2021).

ENSO occurrence and intensity are also markedly influenced by episodic westerly wind bursts (WWBs), a high-frequency disturbance whose time scales are much shorter than a season (Harrison and Giese 1991; Harrison and Vecchi 1997; Seiki and Takayabu 2007). WWBs typically last from several days to a few weeks, and can excite eastward-propagating downwelling Kelvin waves that alter the thermocline structure, thereby affecting both local and remote SST and heat content in the tropical Pacific (Drushka et al. 2015; Lengaigne et al. 2002; McPhaden et al. 1988; McPhaden and Yu 1999). Observations and numerical simulations indicate that when the tropical Pacific warm pool expands eastward or the sea surface is relatively warm, the probability and intensity of WWBs increase—especially during extreme El Niño events (e.g., 1982/83, 1997/98, 2015/16; Fig. 2)—exhibiting a strong state-dependent character (Fedorov et al. 2015; Gebbie et al. 2007; Hu and Fedorov 2019; Lian and Chen 2021; Puy et al. 2019; Yu and Fedorov 2022). Thus, WWBs act both as high-frequency stochastic forcing within ENSO dynamics and, under favorable background conditions, can be amplified via the Bjerknes positive feedback to participate in ENSO's low-frequency evolution (Eisenman et al. 2005; Ji et al. 2023).

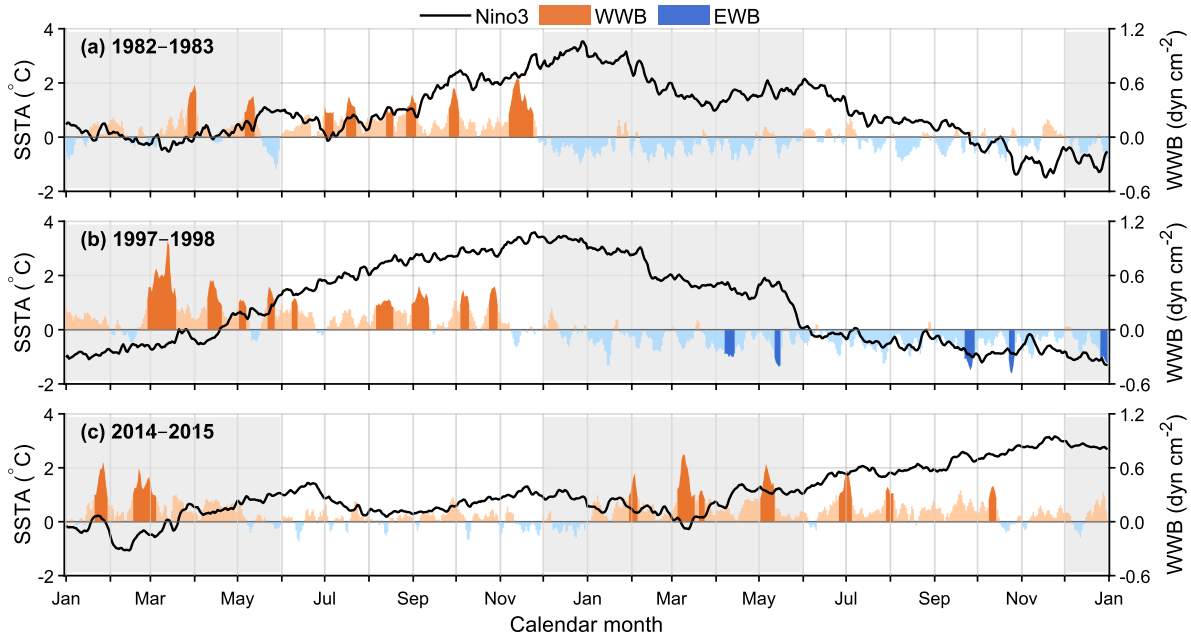

FIG. 2. Observed Niño-3 SSTA (black; °C) and equatorial wind-stress anomalies (shading; dyn cm^{-2}) during canonical strong El Niño events. Wind-stress anomalies are zonally averaged over 120°–180°E and meridionally averaged over 5°S–5°N; orange (blue) shading denotes westerly (easterly) anomalies, with darker tones indicating WWB (EWB). The gray band marks Dec. 1–May 31 period. (a) 1982–1983; (b) 1997–1998; (c) 2014–2015. This figure serves as observational motivation—that summer–autumn WWBs tend to align with accelerated warming whereas spring effects are weaker.

There has long been debate on how the WWB timing relates to ENSO development. One line of research—based on case studies and ensemble sensitivity experiments—argues that WWBs in the early spring, such as the March 1997 event (Fig. 2b), can provide the initiating conditions for extreme El Niño events; the mechanism is that Kelvin waves triggered in spring can reach the eastern Pacific by early summer, laying the groundwork for rapid warming (Chen et al. 2015; Chiodi and Harrison 2017; Lengaigne et al. 2002, 2004; Lian and Chen 2021; Menkes et al. 2014). Conversely, another line of research contends that summer–autumn WWBs (Figs. 2a, c) are more likely to couple with the seasonally sensitive window and, via the local Bjerknes feedback, can efficiently propel ENSO toward its mature phase (Hu and Fedorov 2019; Puy et al. 2019; Yu and Fedorov 2020, 2022). In addition, some studies emphasize the conditional nature of the timing effect: whether a WWB influences subsequent ENSO development depends on the contemporaneous background conditions (e.g., thermocline depth, warm-water volume, and the position of the warm pool) (Drushka et al., 2015; Eisenman et al., 2005; Gebbie et al., 2007; Puy et al., 2016). In sum, because the SST response to a WWB depends not only on the characteristics

of the event itself but also on the background state, observations and numerical models often struggle to isolate the WWB "timing effect."

To date, there is no unified fundamental understanding of how WWB timing influences ENSO. WWBs and ENSO do not stand in a deterministic causal relation—WWBs are neither necessary nor sufficient for ENSO to occur—yet they are dynamically important and cannot be ignored. The SPB framework offers a physical clue to WWB "timing sensitivity": because the seasonal growth rate of the tropical Pacific coupled system is lowest in boreal spring (Fig. 1b), a WWB—as an external forcing—should also induce the weakest SSTA during spring. Put differently, does the oceanic response to WWBs exhibit a "Spring Barrier," such that only WWBs occurring after spring can exert a marked influence on SST development in the central–eastern Pacific? These are the questions this study seeks to answer.

A common feature in Fig. 2 is that WWBs are denser and more persistent in summer–autumn and co-seasonal with accelerated warming, whereas the sustained effect of a single early-spring WWB is comparatively limited. This motivates our analytical treatment of the "WWB timing effect" within the recharge–discharge framework. We develop a conceptual model in which a single WWB is idealized as a finite-duration pulse forcing on SST. We deliver (i) closed-form solutions for a single WWB, (ii) a physical partition of the total response into a same-frequency direct term (phase organizer) and a delayed adjustment term (amplitude controller), and (iii) testable diagnostics identifying when WWBs are most effective, including the vanishing of timing effects under constant growth. We propose the concept of a "WWB Spring Barrier": all else being equal, WWBs that occur in boreal spring experience a systematic reduction in amplification because the background growth rate is lower, yielding a spring–barrier-like weakening of impact; by contrast, WWBs in summer–autumn are more likely to promote ENSO growth.

This paper is organized as follows. Section 2 describes the conceptual model, methods, and data. Section 3 analyzes how WWBs affect ENSO development and elucidates the underlying mechanisms using both analytical and numerical solutions. Section 4 concludes with a summary and discussion. Detailed derivations of analytical solutions are provided in Appendices A and B.

2. Model, method and data

2.1. Conceptual Model

The model builds upon the recharge-discharge oscillator framework (Jin, 1997; Stein et al., 2014) with one key modification: instead of representing high-frequency wind variability as a stochastic forcing, we explicitly prescribe a finite-duration, sudden perturbation $F(t)$ mimicking an individual intense wind burst that act directly on the equatorial Pacific. $F(t) > 0$ represents WWB, while $F(t) < 0$ represent easterly wind burst (EWB). The equations are written as:

$$\begin{cases} \frac{dT}{dt} = R(t)T + \omega_0 h + F(t) \\ \frac{dh}{dt} = -\omega_0 T \end{cases} \quad (1)$$

where T is SSTA in the eastern equatorial Pacific and ω_0 is the frequency of ENSO; $R(t) = R_0 - R_1 \sin(\omega_1 t + \varphi)$ is the seasonally varying growth rate with annual frequency $\omega_1 = \frac{2\pi}{12}$ month^{-1}, which contributes to the phase locking of ENSO variance (Chen and Jin 2020) and SPB (Levine and McPhaden 2015); h is a proxy for thermocline depth anomalies in the zonal mean (120°-280°E) equatorial Pacific expressed in temperature units; it effectively represents anomalies of the upper-ocean heat capacity (Meinen and McPhaden 2000). To convert h to a depth perturbation z, h can be multiplied by a scaling factor $\frac{H_0}{T_0}$ (m°C^{-1}), i.e., $z \approx \frac{H_0}{T_0} h$, where H_0 and T_0 are roughly 200 m and 25°C, representing the mean thermocline depth in the zonal mean equatorial Pacific and the depth-weighted mean temperature above the thermocline, respectively.

Figure 3 shows the numerically obtained time-series of SSTA, thermocline depth and the ACC of SSTA, based on Eq. (1) with $F(t) = 0$. We set $R_0 = 0,\ R_1 = 0.19$ month^{-1} and $\varphi = \frac{2\pi}{12}$ rad, $\omega_0,\ \omega_1 = \frac{2\pi}{48}, \frac{2\pi}{12}$ month^{-1}, respectively. The theoretical model clearly reproduces the SSTA SPB (Fig. 3b), consistent with observations (Fig. 1c) and as analyzed in detail by Jin and Liu (2021). In what follows, we use the SSTA series in Fig. 3a as the background state for the WWB experiments.

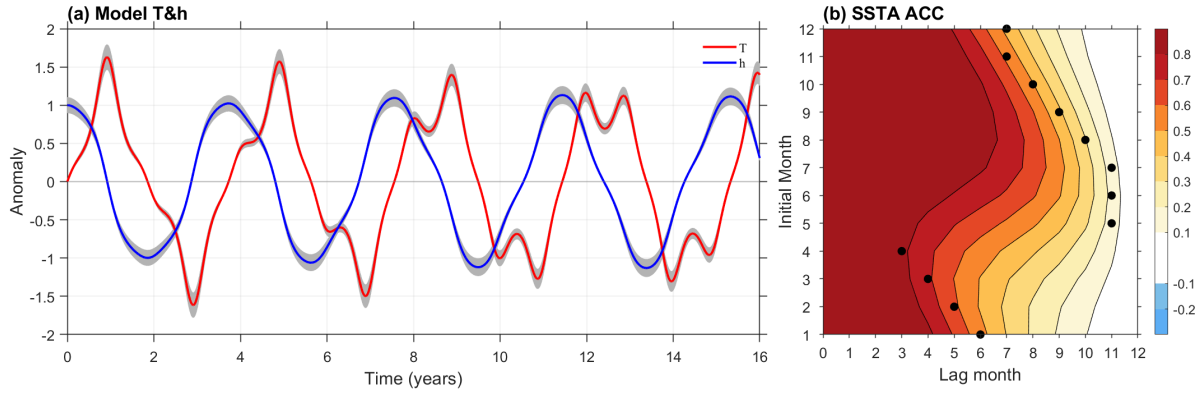

FIG. 3. Numerical solution of Eq. (1) without external forcing. (a) Niño-3 SSTA (red curve) and thermocline depth anomaly (blue curve) in the equatorial Pacific; (b) the SSTA ACC similar to Fig. 1c. Parameters used here are $R_0 = 0, R_1 = 0.19$ month^{-1} and $\varphi = \frac{2\pi}{12}$ rad, ω_0, $\omega_1 = \frac{2\pi}{48}, \frac{2\pi}{12}$ month^{-1}. Initial conditions are $T(t=0) = 0$ and $h(t=0) = 1$. 100 ensemble experiments are done with the initial $h(t=0) \in [0.9, 1.1]$, denoted by grey shadow in (a), where the thick curves are for ensemble mean.

The external perturbation $F(t)$ is given by a finite rectangular pulse

$$F(t) = F_0 \cdot M(t), \qquad M(t) = H(t - t_0) \cdot H(t_0 + \Delta t - t) \tag{2}$$

where,

$$H(t - t_0) = \begin{cases} 0, & t < t_0 \\ 1, & t \geq t_0 \end{cases}, \quad H(t_0 + \Delta t - t) = \begin{cases} 0, & t > t_0 + \Delta t \\ 1, & t \leq t_0 + \Delta t \end{cases}$$

are the Heaviside step function, F_0 the pulse amplitude (units: °C/month), t_0 the onset timing, and Δt the duration. In this paper WWBs are treated as purely exogenous, weather-scale disturbances whose occurrence and amplitude are independent of the ENSO state. Each event is implemented directly as the deterministic rectangular pulse defined above.

Our analysis targets the conditional timing effect—how SST responses differ by WWB timing given that a WWB occurs. Although WWB generation may be random, semi-stochastic or state-dependent (Alam et al. 2023; Alam and Tang 2021; Fedorov and Hu 2016; Gebbie et al. 2007; Hu and Fedorov 2019; Lian and Chen 2021; Liu et al. 2025; Puy et al. 2015, 2016, 2019; Seiki and Takayabu 2007; Tan et al. 2020), our conclusions apply at the event level conditional on occurrence: once a WWB happens, the seasonal background growth rate governs the ensuing amplification or decay.

All numerical simulations are conducted with a time step of 4 hours, a disturbance duration $\Delta t = 15$ days, and a disturbance intensity $F_0 = 1$°C/month. We see that in Fig. 2 a fairly strong WWB (e.g., ~0.5 dyn cm^{-2}) persisting for 15-30 days aligns with the Niño-3 SST rise by roughly 1.0°C. This is an upper-bound scaling. Without asserting causality—and under a "most-favorable" assumption that a given WWB is the sole driver, we think $F_0 = 1$°C/month is a reasonable value representing the maximum SST change that a month-long WWB could produce.

2.2. Definition of perturbation response

The perturbed solution of the system is denoted by (T, h), while the unperturbed solution (with $F(t) = 0$) is denoted by $(\bar{T},\ \bar{h})$. A short disturbance occurs at time t_0 and lasts for a duration Δt. The ending time of the disturbance is set as t_1 $(= t_0 + \Delta t)$. The *instantaneous response* of the system is defined as the immediate difference at the end of the disturbance:

$$\Delta T(t_1) = T(t_1) - \bar{T}(t_1),\ \ \Delta h(t_1) = h(t_1) - \bar{h}(t_1) \tag{3}$$

To quantify the system's response over a finite period t_2 following the disturbance, we define the *adjustment or delayed response* as the difference between the perturbed and unperturbed solutions:

$$\Delta T(t_1 + t_2) = T(t_1 + t_2) - \bar{T}(t_1 + t_2),\ \ \Delta h(t_1 + t_2) = h(t_1 + t_2) - \bar{h}(t_1 + t_2) \tag{4}$$

2.3. Observational data for ENSO and WWB identification

Three observed SST datasets are used in Figs. 1-2: (1) Extended Reconstructed SST Version 6 (ERSSTv6) (Huang et al. 2025) – monthly SST at 2° × 2° resolution. (2) Hadley Centre Global Sea Ice and SST dataset (HadISST) (Rayner et al. 2003) – monthly SST at 1° × 1° resolution. (3) NOAA Optimum Interpolation SST version 2 (OISSTv2) (Huang et al., 2021) – High-resolution daily SST at 0.25° × 0.25° resolution. For each dataset, SST anomalies are computed by removing the climatological annual cycle (monthly climatology for monthly datasets; daily climatology for daily datasets) over the base period 1982–2011. The Niño indices are defined as the area-mean SST anomaly over the standard equatorial region (5°S–5°N): Niño-3 (150°W–90°W) and Niño-3.4 (170°W–120°W).

To identify WWB event in Fig. 2, we use daily 10-m wind fields from the ERA5 reanalysis dataset provided by the European Centre for Medium-Range Weather Forecasts (ECMWF) (Hersbach et al. 2020), with a spatial resolution of 0.25°×0.25°. Daily zonal and meridional winds (u and v, respectively) are converted to zonal surface wind stress using a bulk formula:

$$\tau_x = \rho_a C_D \sqrt{u^2 + v^2} u \tag{5}$$

where ρ_a (air density) and C_D (drag coefficient) are taken as 1.25 kg m^{-3} and 1.3×10^{-3}, respectively. Wind stress anomalies are obtained by subtracting the daily climatology (base period 1995–2005) so that the resulting indices reflect departures from the seasonal cycle.

We define a zonal wind-stress index, $\tau_{x-index}$, by averaging zonal wind stress anomalies over the equatorial Pacific region from 120°E-180°E and 5°S-5°N. This index contains both intra-seasonal and interannual variability. To distinguish WWBs and EWBs, we construct two variants of the index by, prior to averaging, retaining only positive (for WWBs) or only negative (for EWBs) wind-stress anomaly values within the domain.

WWBs or EWBs are detected when both of the following criteria are satisfied (Fig. 2): (i) the magnitude of $\tau_{x-index}$ exceeds 1.5 times the mean standard deviation of the index, (ii) the anomaly persists for at least 5 consecutive days. This thresholding and duration criterion identifies events that are both strong and sustained. Our approach to defining anomalies relative to the annual cycle follows previous studies (Hu and Fedorov 2016; Yu and Fedorov 2020).

3. Analytical solution vs. numerical result

3.1. Instantaneous response

In this section, we derive an analytical solution for the instantaneous response to quantify the immediate Niño-3 SST impact of WWBs occurring at different times of the year. Because the observed mean growth rate $R_0 = 0.0007\ \text{month}^{-1}$ is extremely small, we set $R_0 = 0$ for simplicity, so that the background growth rate is represented as a purely annual-cycle form, i.e.,

$$R(t) \approx -R_1 \sin(\omega_1 t + \varphi) \tag{6}$$

Here, φ is the initial phase of the annual cycle, defined relative to 1 January. From observations, R_1, ω_1 and φ are estimated to be $0.19\ \text{month}^{-1}$, $\frac{2\pi}{12}\ \text{month}^{-1}$ and $\frac{\pi}{6}$, respectively (Fig. 1).

For a short-duration WWB pulse forcing with amplitude F_0 and duration Δt (Eq. 2), a perturbation approach (An and Jin 2011; Chen and Jin 2020) yields an analytical solution for the instantaneous response (see Appendix A for details):

$$\Delta T(t_0+\Delta t) = \frac{F_0}{\omega_0}\sin(\omega_0\Delta t) + \frac{R_1F_0}{2\omega_0}[A\sin(\Omega_1\Delta t+\Phi) - B\sin(\Omega_2\Delta t+\Phi)$$

$$-(A-\mathrm{B})\sin(\Phi)\cos(\omega_0\Delta t) - \left(\frac{\Omega_1}{\omega_0}A - \frac{\Omega_2}{\omega_0}B\right)\cos(\Phi)\sin(\omega_0\Delta t)] \quad (7)$$

where, $\Omega_1 = \omega_1 - \omega_0,\ \Omega_2 = \omega_1 + \omega_0,\ \Phi = \omega_1 t_0 + \varphi,\ A = \frac{\omega_1-\omega_0}{\omega_0^2-(\omega_1-\omega_0)^2},\ B = \frac{\omega_1+\omega_0}{\omega_0^2-(\omega_1+\omega_0)^2}$.

Assuming the WWB duration satisfies $\Delta t \ll 1/\omega_1$, Eq. (7) can be Taylor-expanded for small Δt, yielding the simplified solution:

$$\Delta T(t_0+\Delta t) \approx F_0\Delta t\cdot\left(1+\frac{1}{2}R(t_0)\Delta t\right) \quad (8)$$

Correspondingly, the instantaneous response of the tropical Pacific thermocline depth anomaly is given by:

$$\Delta h(t_0+\Delta t) \approx -F_0\omega_0\Delta t^2\cdot\left(\frac{1}{2}+\frac{1}{6}R(t_0)\Delta t\right) \quad (9)$$

Eq. (8) has a much clearer and simpler physical interpretation than Eq. (7). It shows that the instantaneous SST response to a short WWB consists of two main contributions. The first term on the right-hand side, $F_0\Delta t$, is the linear response to the forcing and increases linearly with the duration. The second term, $\frac{1}{2}F_0R(t_0)\Delta t^2$, represents the modulation of the instantaneous response by the seasonal cycle of the coupled system; its magnitude is entirely controlled by the background growth rate $R(t_0)$ at the WWB timing. Observations indicate that R reaches a minimum in March and a maximum in September (Fig. 1b). Therefore, the instantaneous warming induced by spring WWBs is weakest, whereas that induced by autumn WWBs is strongest. In other words, WWB impacts on ENSO development may also exhibit a spring barrier.

Figure 4 illustrates the instantaneous SST response to WWBs. First, the numerical solution of Eq. (1) (solid) is almost indistinguishable from the analytical solution of Eq. (7) (Fig. 4b, dotted), indicating that the analytical solution accurately captures the WWB-induced instantaneous response. Second, the simplified analytical solution from Eq. (8) (dashed) agrees closely with Eq. (7), demonstrating that Eq. (8) retains the essential mechanism: the instantaneous response

amplitude is set by the contemporaneous background growth rate $R(t_0)$, yielding a "weakest in spring, strongest in autumn" seasonal phase that matches $R(t)$ (gray shading in Fig. 4b). At this short time scale, the negative thermocline feedback has not yet had time to act. In Fig. 4a, each tick marks a WWB timing, with tick length indicating the response magnitude; downward ticks denote EWBs. Importantly, the "spring-minimum, autumn-maximum" seasonality of the instantaneous response is independent of the SST state on January 1 (i.e., independent of the ENSO initial phase).

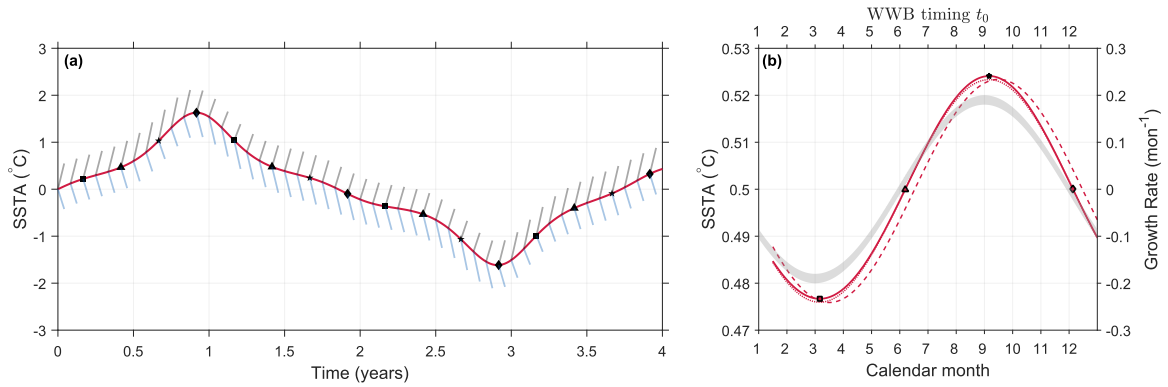

FIG. 4. Instantaneous SST response (units: °C) to the WWB. (a) Niño-3 SSTA evolution in a 4-year time frame in undisturbed control run. The tick shows the WWB timing and each tick corresponds to a disturbed run. (b) Changes of SSTA (red) with the WWB timing and the background growth rate $R(t)$ (grey shadow, units: month^{-1}). Solid, dotted and dashed curves represent the numerical, analytical and simplified analytical results, respectively. Forcing parameters are $F_0 = 1$°C/month, $\Delta t = 0.5$ month. Other parameters used here are same as those in Fig. 3.

Two observational facts are relevant here: (i) $|R(t)| < 0.5/month$ (Fig. 1b), and (ii) a single WWB typically has a duration $\Delta t < 1\ month$ (Fig. 2). Together, these conditions ensure that the factor $1 + \frac{1}{2}R(t_0)\Delta t > 0$ in Eq. (8). This yields a directional result: regardless of the phase of tropical SST evolution, the instantaneous response to an individual WWB is always positive, i.e., it increases Niño-3 SSTA and thus favors El Niño development. The difference lies only in the magnitude, which depends on timing—smallest in spring and largest in autumn. Put differently, the instantaneous response is the "immediate push" that a WWB gives to the system toward the warm state; how effective that push depends on whether the system at that time is in an "amplifying" regime ($R(t_0) > 0$ and large) or a "braking-dominated" regime ($R(t_0) \leq 0$).

These conclusions have a mirror symmetry for EWBs. Under the same $R(t)$ and Δt, reversing the sign of the forcing (i.e., replacing the positive WWB pulse by a negative EWB pulse) leads to an instantaneous response that is always negative: an EWB reduces Niño-3 SSTA regardless of the ENSO phase. The seasonal dependence is likewise preserved, with the weakest cooling in spring and the strongest cooling in autumn, that is, EWBs tend to suppress El Niño and favor La Niña, with their timing dependence also governed by the annual cycle of the background growth rate.

3.2. Adjustment response

We are more concerned with the persistent impact of WWBs. Appendix B provides the detailed derivation of the analytical solution for the adjustment response. In brief, it consists of two components:

$$\Delta T(t_1 + t_2) \approx \Delta T_0(t_2) + R_1\,\Delta T_1(t_2)$$
$$= R_c\cos(\omega_0 t_2 - \psi) + R_1 M(\theta)\cos(\omega_0 t_2 - \psi - \gamma(\theta)) \quad (10)$$

Here, $R_c = \sqrt{C_1^2 + C_2^2}$ is constant, $C_1 = F_0\Delta t$, $C_2 = -\frac{1}{2}F_0\omega_0\Delta t^2$, $\psi = \mathrm{atan2}(C_2, C_1)$, $\theta = \omega_1(t_1 + t_2) + \varphi$ is seasonal phase, $M(\theta)$ and $\gamma(\theta)$ are given by Eq. (B12).

$\Delta T_0(t_2)$ and $\Delta T_1(t_2)$ are given by Eqs. (B5) and (B12), respectively, in Appendix B. We refer to them as the free same-frequency response and the seasonally modulated adjustment response over the lag t_2 period following a WWB. $\Delta T_0(t_2)$ arises from phase propagation at the intrinsic ENSO frequency ω_0 over the lag time t_2: it represents the free evolution of the instantaneous WWB-induced SST perturbation and is independent of the first-order modulation by the background growth rate. Its amplitude R_c is determined solely by the WWB strength and duration. In contrast, $\Delta T_1(t_2)$ describes the continued evolution after the WWB under the modulation of the seasonal growth rate via the Bjerknes feedback, and can be interpreted as a convolution of the oceanic thermocline adjustment with the seasonal gain. Its amplitude $M(\theta)$ and phase shift $\gamma(\theta)$ depend explicitly on the seasonal phase θ, highlighting the sensitivity of the adjustment response to WWB timing.

In the real world, how long the persistent impact of WWBs can last remains highly debated. For simplicity, we examine SST evolution over a fixed window of $t_2 = 12$ months following a

WWB. Figure 5 shows the SST trajectories in a two-year framework for WWBs occurring at different calendar months t_0 (January–December). Figure 5a first demonstrates that the analytical solution (Eq. 10) agrees closely with the numerical integration: for each WWB timing, the two curves nearly overlap, with only small amplitude differences. This indicates that Eq. (10), derived within the recharge–discharge framework, accurately captures the coupled effects of thermocline adjustment and the Bjerknes feedback. Regardless of WWB timing, the SSTA reaches a maximum in late autumn to early winter (November–December), clearly reflecting ENSO's seasonal phase locking. In contrast, the response is strongly clamped in late spring to early summer (May–June), consistent with a spring barrier in SST development, in agreement with previous studies (Levine and McPhaden 2015; Liu et al. 2019; McPhaden 2003; Webster and Yang 1992; Zheng and Zhu 2010).

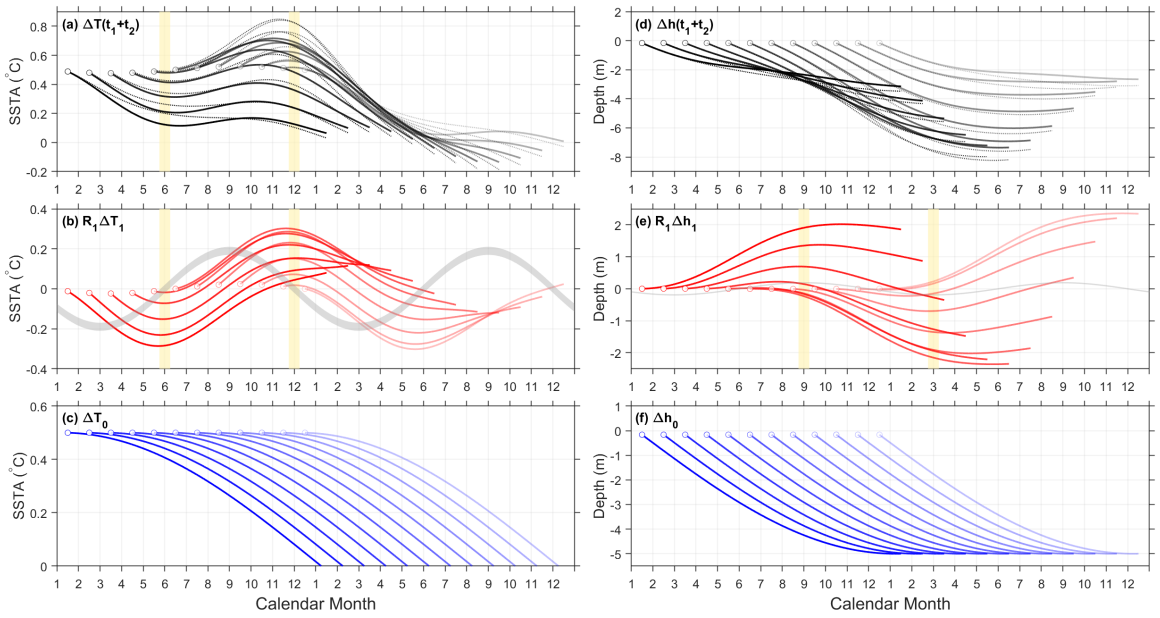

FIG. 5. Adjustment responses of Niño-3 SSTA (left column, units: °C) and thermocline depth anomaly in the equatorial Pacific (right column, units: m) to the WWBs in a 2-year timeframe. The abscissa is the calendar month starting from January 1. (a) Total SSTA response $\Delta T(t_1 + t_2)$. Each solid (analytical) and dotted (numerical integration) curve is a realization for a WWB initiated on the first day of a given month, with the open circle denoting the WWB timing. The first WWB occurs at January 1 (first open circle from the left) and lasts 15 days; subsequent open circles marks WWBs on the first day of each month from February 1 through December 1. (b) Seasonally modulated component $R_1\Delta T_1$ (red); the background growth rate $R(t)$ is shown by the grey curve (units: month^{-1}). (c) Direct same-frequency component ΔT_0 (blue). (d)-(f) Same as (a)-(c), but for thermocline depth anomaly. Positive (negative) value denotes deepening (shoaling) of the thermocline depth. Vertical orange shading marks the calendar windows of peak SSTA, where $R(t) = 0$. Forcing parameters: $F_0 =$ 1°C/month. Other parameters are the same as in Fig. 3.

As anticipated from Eq. (10), the phase of the total SSTA response is controlled primarily by the seasonally modulated adjustment component. Figure 5b directly illustrates how the amplitude of this modulated component varies with seasonal phase. During June–December, when the seasonal growth rate is positive ($R > 0$), the convolution of the oceanic thermocline adjustment with the seasonal gain leads to a pronounced accumulation, causing SSTA to reach its maximum in late autumn to early winter. By contrast, during January–June, when the growth rate is negative ($R < 0$), the same accumulation acts in the opposite sense and produces a minimum around the late-spring to early-summer transition. Figure 5c shows that the direct (same-frequency) response triggered by WWBs in different months has an almost identical evolution and is independent of WWB timing. This reflects the free propagation of the WWB-induced perturbation at the intrinsic ENSO frequency ω_0, which is independent on the contemporaneous seasonal growth rate, thereby providing an oscillatory baseline for the total response.

Figure 5b also indicates that, all else being equal, WWBs occurring after early summer are more readily amplified through the Bjerknes feedback and can accumulate across seasons, thereby playing a key role in driving an event toward maturity. In contrast, most winter–spring WWBs are effectively "clamped" by the weak background growth rate in spring and therefore struggle to produce sustained warming. This timing dependence of SST evolution on WWBs is consistent with observations from major events such as 1982/83, 1997/98, and 2015 (Fig. 2): extreme years are typically accompanied by frequent and/or persistent WWBs during summer–autumn, whereas isolated early-spring WWBs alone are usually insufficient to push an event to extreme amplitude (Hu and Fedorov 2019; Puy et al. 2019; Yu and Fedorov 2020).

The seasonal evolution of the tropical Pacific thermocline depth exhibits an approximate quarter-cycle phase difference relative to Niño-3 SSTA, corresponding to a lag of about $\pi/2$ (roughly three months). When Niño-3 SSTA reaches a minimum in late spring and a maximum in late autumn (Fig. 5b), the thermocline subsequently deepens in late summer and shoals in late winter, respectively (Fig. 5e). This phase relationship is characteristic of the tropical thermocline–SST recharge–discharge mechanism (Jin, 1997) and will not be discussed further here.

Finally, the close agreement between the analytical and numerical solutions demonstrates that the closed-form representation of "a single intrinsic frequency plus seasonal modulation" captures the essential physics of the WWB timing effect. The former provides the free same-frequency baseline, while the latter represents the modulation gain driven by the seasonal growth rate. Their

superposition yields a realistic amplitude–phase structure and seasonal phase locking of the total response. Under the model configuration and parameters used here, if the persistent influence of a WWB is assumed to last up to 12 months, the WWB timing determines whether its effect can cross the spring barrier and be amplified within the summer–autumn window. In this sense, the result represents an event-scale manifestation of the seasonal phase locking and the SPB in ENSO development.

It is also important to note that these characteristics of the adjustment response are independent of the SST state on January 1 (i.e., independent of the initial ENSO phase). The conclusions likewise exhibit mirror symmetry for EWBs: regardless of when an EWB occurs during the SST evolution, the adjustment response always reduces SSTA, with a seasonal phase characterized by weakest cooling in late spring–early summer and strongest cooling in late autumn–early winter (Fig. 6).

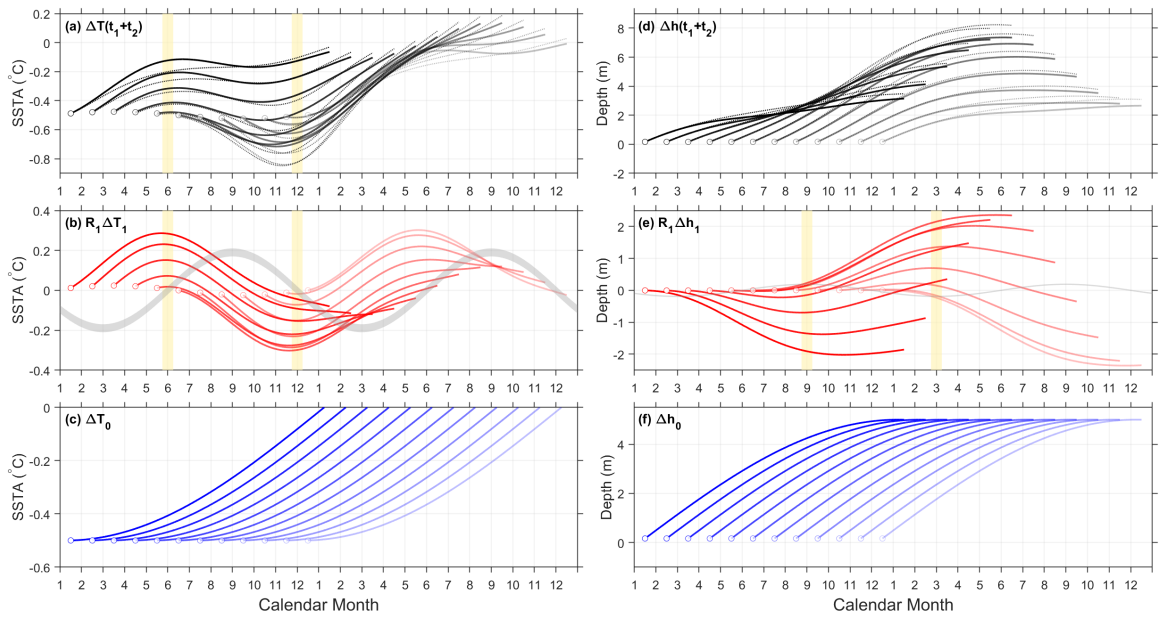

FIG. 6. Same as Fig. 5, but for adjustment responses to the EWBs.

If the potential influence timescale of a WWB is assumed to be small compared with the ENSO period (taken here as 4 years), i.e., $t_2 \ll 1/\omega_0$, then the trigonometric terms involving $\omega_0 t_2$ in the analytical solution can be expanded in a Taylor series with respect to t_2. Under the zeroth-order approximation, the complicated analytical solution Eq. (10) can be simplified as:

$$\Delta T(t_1+t_2) \approx F_0 \Delta t \cdot \left[1 + \frac{1}{2} R(t_0)\Delta t + \int_{t_1}^{t_1+t_2} R(\tau)d\tau\right] \quad (11)$$

When $t_2 = 0$, Eq. (11) reduces to Eq. (8). Under the zeroth-order approximation, the adjustment response is therefore determined primarily by the cumulative effect of the background growth rate $R(t)$ over the interval t_2, and is independent on the intrinsic ENSO frequency ω_0. It should be noted that the full analytical solution derived in Appendix B contains terms that depend explicitly on ω_0; however, these ω_0-related terms become negligible for a short t_2.

Unlike Figs. 5–6, Fig. 7 shows the SSTA at the t_2-th month after a WWB, with the upper abscissa indicating the timing of the WWB. First, the approximate analytical solution derived from Eq. (11) (blue dashed) is nearly identical in phase to the numerical solution obtained from Eq. (1) (black solid). The adjustment response of SST is also largely determined by the contemporaneous background growth rate R: when R weakens during winter–spring, the SSTA induced by a WWB is weakest; after spring, as R gradually strengthens, the WWB-induced SSTA correspondingly increases; and WWBs occurring in summer–autumn produce the strongest SSTA. Within the short timescale of $t_2 = 1 - 3$ months (Figs. 7a–c), the amplitudes of the analytical and numerical solutions are also nearly identical, indicating that the analytical solution Eq. (11) accurately captures the short-term response induced by WWBs. Therefore, from a short-term perspective, the spring barrier of WWBs is essentially analogous to the ENSO SPB: both arise from the modulation by the seasonal cycle of the background growth rate in the tropical coupled ocean–atmosphere system.

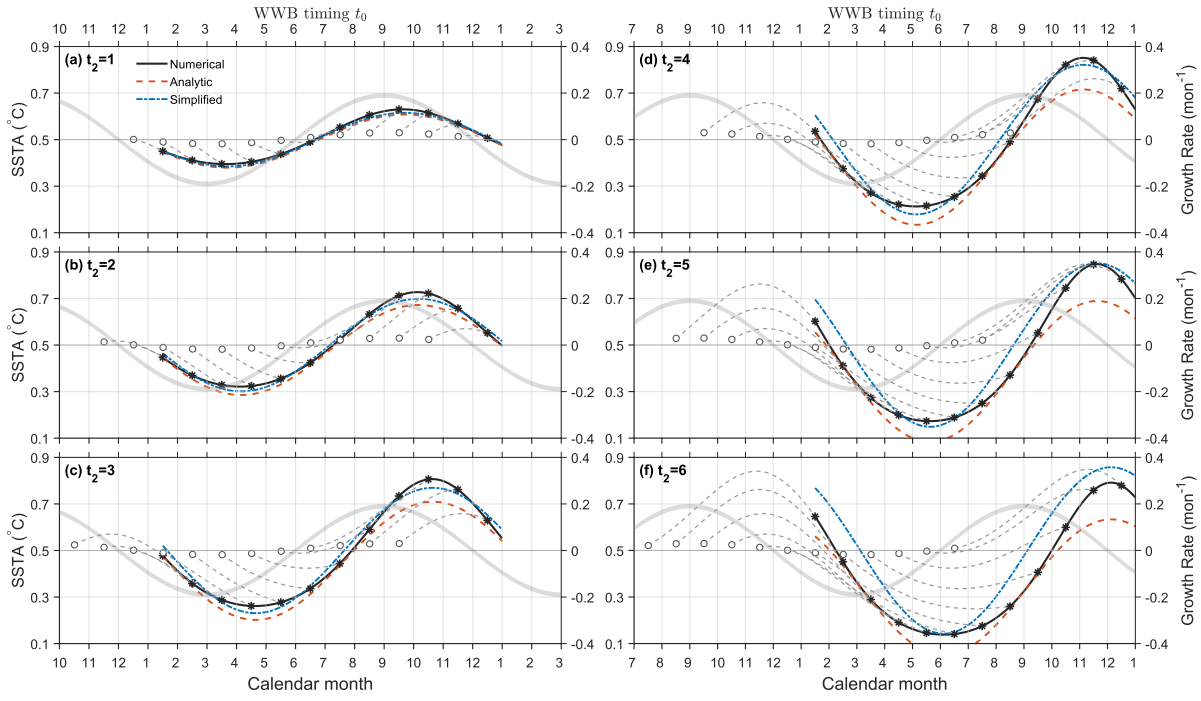

FIG. 7. Adjustment response of Niño-3 SSTA (units: °C) to the WWB at (a)-(f) $t_2 = 1$, 2, 3, 4, 5 and 6 month. The background growth rate $R(t)$ (units: month^{-1}) is shown by grey curve (right axis). The upper

abscissa denotes the WWB timing t_0; the lower abscissa is the calendar month starting from October 1. In (a), the first WWB occurs at December 1 (first open circle from the left) and lasts 15 days; the $t_2 = 1$ month response is therefore evaluated on January 15 (first asterisk from the left). The dashed segment between the circle and the asterisk indicates the 1-month SST evolution. Subsequent open circles marks WWBs on the first day of each month from January 1 through November 1. In (b)-(f), the first WWB is set to November 1, October 1, September 1, August 1 and July 1, respectively. Numerical, analytical and simplified-analytical solutions are shown by the solid black, dashed red and dashed blue curves, respectively.

When the response window is extended to $t_2 = 4 - 6$ months (Figs. 7d–f), the phase of SSTA becomes increasingly controlled by the same-frequency direct term associated with the intrinsic ENSO frequency. As a result, the peak response window exhibits a systematic phase delay (i.e., a rightward shift) compared with the $t_2 = 1 - 3$-month cases. The background growth rate still determines the overall amplitude pattern—weakest in spring and strongest in summer–autumn. However, unlike the short-term response, the negative feedback associated with the thermocline (i.e., the ocean dynamical memory) begins to significantly suppress the amplitude. Consequently, the numerical solution (black solid) shows smaller amplitudes than the simplified analytical solution (blue dashed), which neglects the thermocline restoring term. Nevertheless, the adjustment response to winter–spring WWBs remains the weakest, indicating that the WWB spring barrier is not confined to the instantaneous response but also persists over subsequent monthly timescales

Overall, the analytical solution, the approximate analytical solution, and the numerical solution exhibit a high degree of consistency in phase, primarily because the seasonal variation of the background growth rate plays a dominant role in determining the phase of response. In terms of amplitude, however, the difference between the approximate analytical solution (blue dashed) and the numerical solution increases as t_2 becomes larger. This discrepancy arises because higher-order terms and the thermocline negative feedback, which are included in the numerical integration, become increasingly important. By contrast, the full analytical solution (red dashed) agrees more closely with the numerical solution (black solid), particularly in Figs. 7e-f.

3.3. Sensitivity of adjustment response to parameters

The parameters affecting the adjustment response include the intrinsic ENSO frequency ω_0, the amplitude of the background growth rate R_1, and its initial seasonal phase φ. In general, ω_0

has little influence on the response amplitude and only slightly adjusts the response phase at longer lags. The parameter R_1 modifies the response amplitude without affecting its phase, whereas φ shifts the seasonal phase in calendar time, thereby altering the timing of ENSO phase locking and the barrier season, but without changing the overall ENSO amplitude. These effects can be readily inferred from Eqs. (10) and (11).

If only the short-term influence of WWBs is considered (e.g., $t_2 = 1-3$ months), Eq. (11) indicates that both the amplitude and phase of the adjustment response are independent of ω_0. Consequently, changing the ENSO period has little effect. Figure 8 shows that when the ENSO frequency is set to $\omega_0 = \frac{2\pi}{36}, \frac{2\pi}{60}$ (corresponding to 3- and 5-year periods, respectively), the resulting adjustment responses are nearly identical to that in Fig. 7c. It is worth noting that when the ENSO period is 5 years, the condition $t_2 \ll 1/\omega_0$ is better satisfied, leading to closer agreement between the simplified analytical solution and the numerical solution (Fig. 8b). When the WWB influence is evaluated up to one year, however, the peak window of the adjustment response shifts by about one month because the phase of the same-frequency direct response depends on $\omega_0 t_2$ (Eq. (10)): relative to the 4-year period, the peak occurs about one month earlier for a 3-year period and about one month later for a 5-year period (figure not shown).

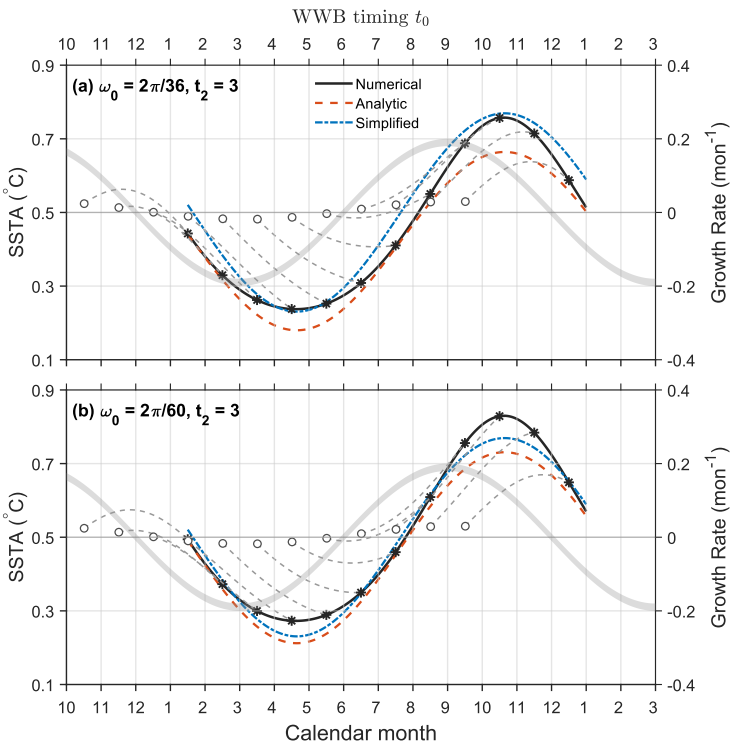

FIG. 8. Same as Fig. 7c, but for (a) $\omega_0 = \frac{2\pi}{36}\ mon^{-1}$ and (b) $\omega_0 = \frac{2\pi}{60}\ mon^{-1}$, respectively.

In the total response $\Delta T \approx \Delta T_0 + R_1 \Delta T_1$, the parameter R_1 acts only as a linear scaling factor for the adjustment component. Increasing (or decreasing) R_1 simply amplifies (or reduces) ΔT_1 and the total peak amplitude proportionally, without altering the timing of the peak or the phase structure of the response, including the positions of autumn–winter phase locking and the spring barrier. Consequently, for a given WWB timing, the response curves should retain the same phase but exhibit different amplitudes when R_1 is varied (figure not shown).

The initial seasonal phase of the background growth rate, φ, is a key control parameter that determines the specific seasons in which the ENSO predictability barrier and phase locking occur. This conclusion has been widely discussed in previous theoretical studies (Chen and Jin 2022, 2020, 2023; Galanti and Tziperman 2000; Levine and McPhaden 2015; Liao et al. 2021; Stein et al. 2010, 2014; Tziperman et al. 1995, 1997; Yang et al. 2023). Figure 9 illustrates that when $\varphi = \frac{\pi}{2}$, corresponding to a two-month leftward shift in the initial phase of $R(t)$, the peak and trough windows of the WWB adjustment response also shift two months earlier. Specifically, the original pattern—weakest warming in late spring–early summer and strongest warming in late autumn–early winter (Fig. 7)—is transformed into weakest warming in late winter–early spring and strongest warming in late summer–early autumn (Fig. 9). This result confirms that the seasonal phase of the background growth rate is the fundamental factor controlling the timing window of WWB climatic effects. In other words, although the overall amplitude of the ENSO response remains largely unchanged, the season in which the response is amplified or suppressed shifts. This indicates that changes in the phase of the annual cycle of tropical SST could have profound implications for ENSO behavior.

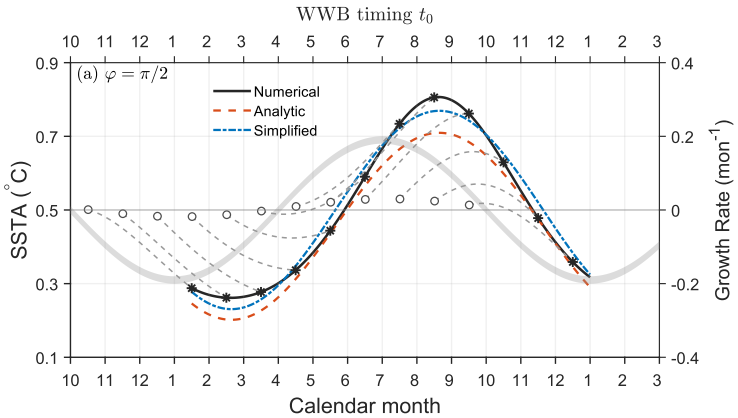

FIG. 9. Same as Fig. 7c, but for $\varphi = \frac{\pi}{2}\ rad$.

In summary, the magnitude of the response induced by a WWB is controlled by R_1, whereas when the response becomes strong or weak is jointly determined by φ and ω_0. Among these factors, φ plays the dominant role, while ω_0 only provides a minor adjustment. Thus, the so-called timing sensitivity—namely, whether a WWB can overcome the spring barrier and be effectively amplified—is primarily governed by the seasonal phase of the background state φ and the instantaneous growth rate $R(t_0)$ at the time of the event. Within this framework, R_1 determines the overall amplification level, whereas the intrinsic system frequency ω_0 only slightly adjusts the timing of the peak response window.

3.4. Persistence map for WWB effect

Finally, we examine the role of WWBs from the perspective of predictability. Figures 10a, c, and e display the time series of the total adjustment response ΔT, the seasonally modulated component $R_1\Delta T_1$, and the same-frequency direct component ΔT_0, respectively, all calculated from the analytical solution Eq. (10). Each panel includes six realizations corresponding to different WWB timings, with colors ranging from dark to light. Figures 10b, d, and f show the corresponding ACC-based persistence maps, where the abscissa denotes lag month and the ordinate denotes initialization month.

The most striking feature is that the predictability structure of the total response derived from the analytical solution closely reproduces the observed pattern (Fig. 10b versus Fig. 1c). This result strongly suggests that wind-triggered perturbations coupled with the seasonal variation of the background growth rate alone are sufficient to reproduce the two key characteristics observed in reality: the SPB and winter phase locking. It also implies that the seasonal cycle of the background growth rate—effectively the seasonal modulation of the Bjerknes feedback—imposes a strong dynamical constraint on ENSO predictability. Regardless of how the tropical coupled system is externally perturbed, these two features are likely to persist. In this sense, WWBs represent only one type of external disturbance; similar conclusions may hold for other forms of pulse-like or stochastic perturbations.

The component decomposition further clarifies the physical origins of the SPB and phase locking. The seasonally modulated component $R_1\Delta T_1$ acts as an “amplitude controller” rather than a source of long-term phase memory (Figs. 10c–d). Relative to the ENSO intrinsic frequency,

$R_1\Delta T_1$ behaves as a high-frequency oscillation with an approximately one-year period. It follows the rhythm of the background seasonal cycle and determines in which season the signal is amplified or suppressed. Because its dominant timescale is about one year, its persistence is very short: the ACC decays rapidly after roughly one month (Fig. 10d), indicating that it cannot provide cross-seasonal memory.

In contrast, the same-frequency direct component ΔT_0 provides the "phase backbone" of the response (Figs. 10e–f). This term is not directly modulated by the seasonal growth rate and supplies a smooth, regular, and long-lived baseline for the phase evolution of the total response. As shown in Fig. 10f, its ACC appears as nearly vertical lines independent of the initialization month, indicating that it carries the system's dynamical memory. This long-lived phase memory forms the physical basis that allows ENSO events to persist and evolve across seasons.

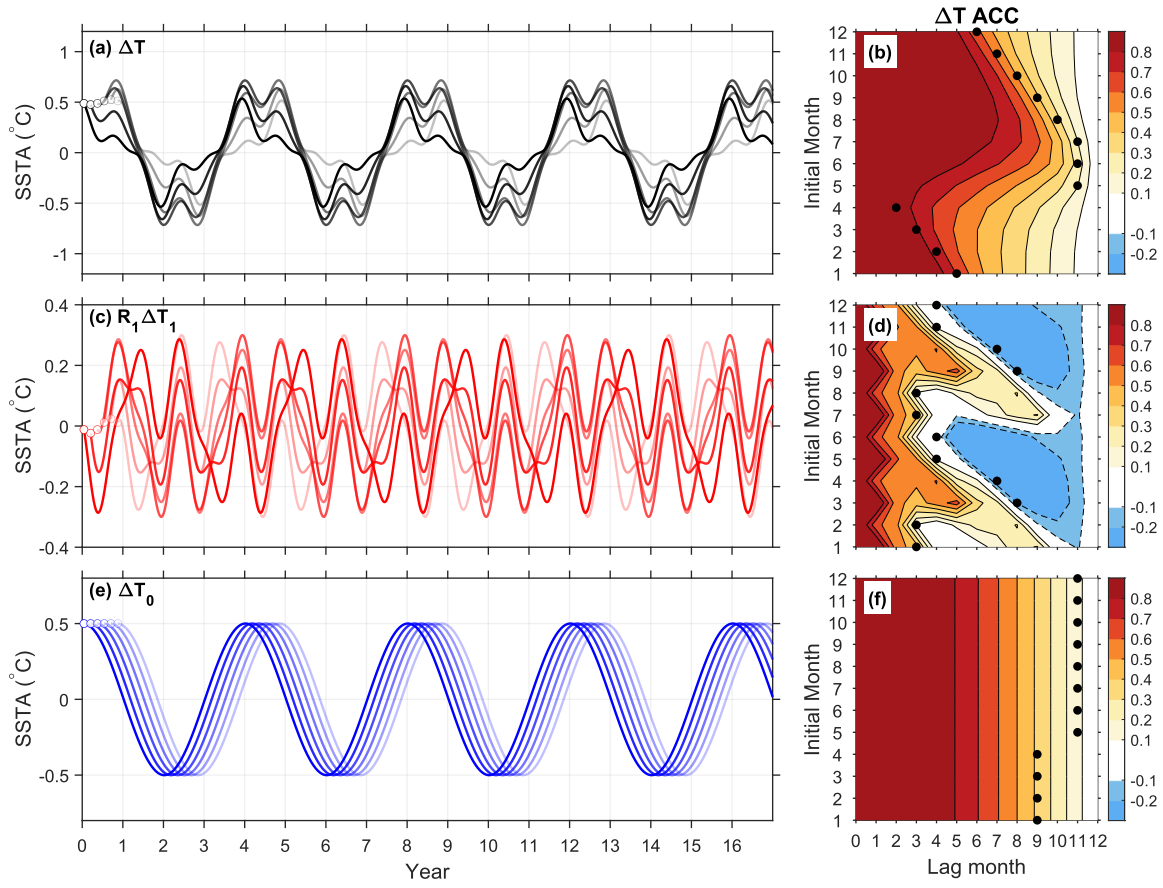

FIG. 10. Analytical solution of Eq. (1) with $F_0 = 1$°C/month that calculated from Eq. (10). (a) Total SSTA response $\Delta T(t_1 + t_2)$ in a 20-year timeframe (i.e., $t_2 = 20\ year$). Each solid curve is a realization for a WWB initiated on the first day of a given month, with the open circle denoting the WWB timing. There are 6 realizations that the WWB occurs at January 1, March 1, May 1, July 1, September 1 and November 1 of year 1, respectively, and lasts 15 days each. (c) Seasonally modulated component $R_1\Delta T_1$ (red). (e) Direct same-

545 frequency component ΔT_0 (blue). (b), (d) and (f) are same as Fig. 1c, but for persistence map calculated from
546 $\Delta T(t_1 + t_2)$, $R_1 \Delta T_1$ and ΔT_0, respectively.

547

548 We summarize this mechanism with the following conceptual expression:

549 $$\text{Total response } \Delta T = \Delta T_0 \text{ (Phase backbone)} + R_1 \Delta T_1 \text{ (Amplitude controller)} \quad (12)$$

550 Physical interpretation:

551 (1) Phase backbone (ΔT_0): Maintains the inertial propagation of the system and provides the
552 dynamical memory that allows an ENSO event, once triggered, to persist across seasons.

553 (2) Amplitude controller ($R_1 \Delta T_1$): Modulates the backbone. It suppresses the amplitude
554 during boreal spring—producing the SPB—and amplifies it during summer–autumn, thereby
555 effectively locking events triggered at different times to reach their peak in early winter.

556 (3) Physical essence of the SPB: In boreal spring, the two components become modulation-
557 mismatched. The memory backbone ΔT_0 tends to maintain the system's ongoing evolution,
558 whereas the amplitude gate $R_1 \Delta T_1$ imposes a strong suppression or negative feedback. This sharp
559 conflict between the persistent phase memory and the seasonal amplitude damping leads to a rapid
560 decay of signal amplitude, which directly manifests as the abrupt collapse of the ACC when
561 crossing spring.

562

563 **4. Summary and discussion**

564 This study derives analytical and numerical solutions for finite-duration WWB pulses within
565 the recharge–discharge oscillator framework and proposes the mechanism of a "WWB Spring
566 Barrier." Under otherwise identical conditions, WWBs occurring in boreal spring exhibit
567 systematically weaker amplification efficiency, whereas those occurring in summer–autumn are
568 most readily amplified by the Bjerknes feedback and can accumulate across seasons, thereby
569 promoting ENSO growth toward its winter peak. This conclusion also exhibits mirror symmetry:
570 EWBs occurring in summer–autumn are likewise most effective in strengthening cold anomalies
571 and sustaining them into winter. Notably, if the seasonal gain of the background state is removed,
572 the timing effect disappears. We emphasize that the mechanism identified here represents a
573 conditional timing effect: given that a WWB has occurred, its subsequent amplification or decay

depends on the season in which it takes place. The analysis does not imply a necessary or sufficient causal relationship between WWBs and ENSO events.

The results also have important implications for ENSO prediction and model diagnostics. WWBs occurring from late summer to early autumn are most easily "captured" by the coupled system, allowing the perturbation to be efficiently amplified and enhancing predictability toward the winter peak. In contrast, WWBs occurring in late winter to spring are more likely to be dissipated by the spring barrier, making it difficult for them to generate sustained impacts even if they occur. The key point is that whether the "energy" injected by a WWB can be converted into predictable growth depends on whether it occurs within the constructive window of the system's response structure, summarized as $\Delta T = \Delta T_0$ (Phase backbone) $+R_1 \Delta T_1$ (Amplitude controller). Accordingly, in forecast analyses, greater weight should be assigned to WWBs occurring in summer–autumn and less weight to those occurring in winter–spring (with EWBs treated symmetrically). This perspective also implies that if a numerical model underestimates the amplitude of the seasonal cycle in the tropical Pacific, it will tend to systematically underestimate the summer–autumn amplification effect of WWBs and the winter phase locking of ENSO, and vice versa.

This study also has several limitations and uncertainties. (1) The derivation relies on linear approximations and small-parameter expansions. Small damping coefficients and short-duration WWB assumptions are adopted to obtain analytical solutions. For situations involving persistent strong forcing, pronounced nonlinearities, or strong state dependence, quantitative estimates of amplitude may deviate from reality; however, the phase evolution (e.g., phase locking and lag relationships) and the seasonal gating mechanism remain informative. (2) The model simplifies several physical processes. It does not explicitly include extratropical forcing, nonlinear interactions between equatorial waves and the mixed layer, or decadal variability in the background state. These processes may modify the seasonal growth rate of the tropical coupled system and thus alter the detailed characteristics of the SPB and seasonal phase locking.

In future work, we will use observations to further test and refine this conceptual framework, with the goal of linking the SPB, seasonal phase locking, and event-scale external forcing within a unified dynamical perspective. Specifically, we will (i) force the conceptual model with observed daily wind stress anomalies and conduct full-wind versus no-wind sensitivity experiments to quantify the contribution of WWBs in representative ENSO events; (ii) extend the framework to include sequences or clusters of WWBs and incorporate stronger nonlinear coupling between the

mixed layer and thermocline, background-state decadal variability, and regional phase differences; and (iii) represent other sources of high-frequency forcing—such as the Madden–Julian Oscillation (MJO) and equatorial wave packets—as equivalent pulse forcings within the same analytical framework, thereby examining how their convolution with seasonal growth rate and thermocline adjustment shapes the amplification and phase delay of ENSO signals.

Acknowledgements:

This research is jointly supported by the NSF of China (Nos. 42288101, 42230403 and 41725021) and by the foundation at the Shanghai Frontiers Science Centre of Atmosphere-Ocean Interaction of Fudan University.

Data Availability Statement:

All data and code used in this study are available upon request.

Conflict of interest:

The authors have no relevant financial or non-financial interests to disclose.

Appendix A: Instantaneous Response

Here we show the details on deriving the analytical expressions for the perturbation responses. First, we denote the perturbed solution by (T, h) and the unperturbed solution by $(\bar{T}, \bar{h})$. Their differences are defined as

$$\Delta T = T - \bar{T}, \quad \Delta h = h - \bar{h}.$$

1. Perturbation Equations

Based on Eq. (1) and Eq. (2), the perturbation equations under the forcing of WWB can be written as:

$$\begin{cases} \Delta\dot{T} = \omega_0 \Delta h - R_1 \sin(\omega_1 t + \varphi)\, \Delta T + F(t) \\ \Delta\dot{h} = -\omega_0 \Delta T \end{cases} \tag{A1}$$

with initial conditions $\Delta T(0) = \Delta h(0) = 0$, $\varphi \in [0, \pi]$. Here, $F(t) = F_0 H(t - t_0) H(t_1 - t)$, that is, $F(t) = F_0 = const.$ for $t_0 \le t \le t_1$, where t_0 is the timing of WWB in a year, $t_1 = t_0 + \Delta t$ is the ending time of WWB, and Δt is the duration of WWB. Usually, Δt can be thought small (less than one month), when compared to a year (or 365 days). ω_0 and ω_1 are the ENSO and annual frequencies and given as $\left(\frac{2\pi}{48}\right)\ month^{-1}$ and $\left(\frac{2\pi}{12}\right)\ month^{-1}$, respectively.

In this paper, we consider a weak seasonal growth rate in the tropical coupled system, i.e., a small R_1, so that ΔT and Δh can be expanded in terms of R_1:

$$\Delta T = \Delta T_0 + R_1 \Delta T_1 + \cdots, \quad \Delta h = \Delta h_0 + R_1 \Delta h_1 + \cdots$$

Therefore, we have

$$\begin{cases} \Delta\dot{T}_0 = \omega_0 \Delta h_0 + F_0 \\ \Delta\dot{h}_0 = -\omega_0 \Delta T_0 \end{cases} \tag{A2}$$

$$\begin{cases} \Delta\dot{T}_1 = \omega_0 \Delta h_1 - \sin(\omega_1 t + \varphi) \Delta T_0 \\ \Delta\dot{h}_1 = -\omega_0 \Delta T_1 \end{cases} \tag{A3}$$

Given initial conditions $\Delta T_0(t_0) = \Delta q_0(t_0) = 0$, the analytical solution to the zeroth-order system (A2) can be obtained:

$$\Delta T_0(t_1) = \frac{F_0}{\omega_0} \sin(\omega_0 \Delta t), \quad \Delta h_0(t_1) = \frac{F_0}{\omega_0} [\cos(\omega_0 \Delta t) - 1]. \tag{A4}$$

644 Substituting the zeroth-order solution (A4) to first-order equations (A3), we have

$$\begin{cases} \Delta\dot{T}_1 = \omega_0 \Delta h_1 - \frac{F_0}{\omega_0} g(t) \\ \Delta\dot{h}_1 = -\omega_0 \Delta T_1 \end{cases} \quad \text{(A5)}$$

646 where, $g(t) = \sin(\omega_1 t + \varphi)\sin\big(\omega_0(t - t_0)\big)$.

647 Eliminating Δh_1 yields

$$\Delta\ddot{T}_1 + \omega_0^2 \Delta T_1 = f(t), \quad f(t) = -\frac{F_0}{\omega_0} g'(t). \quad \text{(A6)}$$

649

650 **2. Decomposition of the forcing and particular solution**

651 Using the identity $\sin A \cdot \sin B = \frac{1}{2}[\cos(A - B) - \cos(A + B)]$, we have

$$\mathrm{g}(t) = \frac{1}{2}\big[\cos\big((\omega_1 - \omega_0)t + \omega_0 t_0 + \varphi\big) - \cos\big((\omega_1 + \omega_0)t - \omega_0 t_0 + \varphi\big)\big]. \quad \text{(A7)}$$

653 This leads to two harmonic forcings:

$$f(t) = \frac{F_0}{2\omega_0}[\Omega_1 \sin(\Omega_1 t + \varphi_1) - \Omega_2 \sin(\Omega_2 t + \varphi_2)]. \quad \text{(A8)}$$

655 where,

$$\Omega_1 = \omega_1 - \omega_0, \quad \Omega_2 = \omega_1 + \omega_0, \quad \varphi_1 = \omega_0 t_0 + \varphi, \quad \varphi_2 = -\omega_0 t_0 + \varphi$$

657 For each harmonic term $f_j(t) = A_j \sin\big(\Omega_j t + \varphi_j\big)$, the particular solution to $T'' + \omega_0^2 T =$
658 $f_j(t)$ is:

$$T_{p,j}(t) = \frac{A_j}{\omega_0^2 - \Omega_j^2} \sin\big(\Omega_j t + \varphi_j\big), \quad \big(\Omega_j \neq \omega_0\big). \quad \text{(A9)}$$

660 Evaluating at $t = t_0 + \Delta t$, we have:

$$\Delta T_{1p}(t_1) = \frac{F_0}{2\omega_0}[A \sin(\Omega_1 \Delta t + \omega_1 t_0 + \varphi) - B \sin(\Omega_2 \Delta t + \omega_1 t_0 + \varphi)] \quad \text{(A10)}$$

662 where,

$$A = \frac{\omega_1 - \omega_0}{\omega_0^2 - (\omega_1 - \omega_0)^2}, \quad B = \frac{\omega_1 + \omega_0}{\omega_0^2 - (\omega_1 + \omega_0)^2}$$

which suggests, for different timing t_0 of WWB, the amplitude of the response does not change.

Adding (A4) and (A10), we have particular solution to $\Delta T(t_0 + \Delta t)$:

$$\Delta T(t_1) = \Delta T_0(t_1) + R_1 \Delta T_{1p}(t_1)$$

$$= \frac{F_0}{\omega_0}\sin(\omega_0 \Delta t) + \frac{F_0}{2\omega_0}[A\sin(\Omega_1 \Delta t + \omega_1 t_0 + \varphi) - B\sin(\Omega_2 \Delta t + \omega_1 t_0 + \varphi)] \quad \text{(A11)}$$

3. Homogeneous correction and full solution

Note that as $\Delta t \to 0$, the particular solution (A11) does not vanish, i.e., $\Delta T_p(t_0 + \Delta t) \neq 0$. Thus, the homogeneous term $\Delta T_{1h}(t) = C\cos(\omega_0 \Delta t) + D\sin(\omega_0 \Delta t)$ is added so that the initial conditions at $t = t_0$ are satisfied. Coefficients C and D are obtained by enforcing:

$$\Delta T_{1p}(t_0) + \Delta T_{1h}(t_0) = 0 \quad \text{(A12)}$$

$$\frac{\partial}{\partial \Delta t}(\Delta T_{1p} + \Delta T_{1h})|_{\Delta t = 0} = 0 \quad \text{(A13)}$$

The full first-order solution is then obtained:

$$\Delta T(t_1) = \Delta T_0(t_1) + R_1\left[\Delta T_{1p}(t_1) + \Delta T_{1h}(t_1)\right]$$

$$= \frac{F_0}{\omega_0}\sin(\omega_0 \Delta t) + \frac{R_1 F_0}{2\omega_0}[A\sin(\Omega_1 \Delta t + \Phi) - B\sin(\Omega_2 \Delta t + \Phi)$$

$$-(A - \mathrm{B})\sin(\Phi)\cos(\omega_0 \Delta t) - \left(\frac{\Omega_1}{\omega_0}A - \frac{\Omega_2}{\omega_0}B\right)\cos(\Phi)\sin(\omega_0 \Delta t)] \quad \text{(A14)}$$

where, $\Phi = \omega_1 t_0 + \varphi$.

4. Asymptotic solution for small Δt

(A14) is too complicated to let us see through the fundamental dynamics. If we consider the short-term WWB, that is, a very small Δt (much shorter than 1 year, i.e., $\Delta t \ll \frac{1}{\omega_1} < \frac{1}{\omega_0}$), we can thus apply Taylor expansions to all sinusoidal terms as:

$$\sin\left(\Omega_{1,2}\Delta t + \Phi\right) = \sin(\Phi) + \Omega_{1,2}\Delta t\cos(\Phi) - \frac{\Omega_{1,2}^2}{2}\Delta t^2\sin(\Phi) + O(\Delta t^3)$$

$$\cos(\omega_0\Delta t) = 1 - \frac{1}{2}{\omega_0}^2\Delta t^2 + O(\Delta t^3), \quad \sin(\omega_0\Delta t) = \omega_0\Delta t + O(\Delta t^3)$$

Substituting them into (A14), yields

$$\Delta T(t_1) = \frac{F_0}{\omega_0}\sin(\omega_0\Delta t) + \frac{-R_1F_0\Delta t^2}{2}\cdot\sin(\omega_1 t_0 + \varphi) + O(\Delta t^3) \quad \text{(A15)}$$

A more compact form of (A15) can be expressed as

$$\Delta T(t_1) = F_0\Delta t\cdot\left(1 + \frac{1}{2}R(t_0)\Delta t\right) + O(\Delta t^3) \quad \text{(A16)}$$

Similarly, we can thus have

$$\Delta h(t_1) = -F_0\omega_0\Delta t^2\cdot\left(\frac{1}{2} + \frac{1}{6}R(t_0)\Delta t\right) + O(\Delta t^4) \quad \text{(A17)}$$

Appendix B: Adjustment Response

We now derive the solution after the WWB forcing has ceased, up to time t_2. This corresponds to the adjustment (or delayed) response of the system during the interval from t_1 to $t_1 + t_2$. In this formulation, $t_0,\ \Delta t,\ t_1$ are given constants, while t_2 is the only variable. The perturbation equations can be written as:

$$\begin{cases} \dot{\Delta T} = \omega_0 \Delta h - R_1 \sin[\omega_1 (t_1 + t_2) + \varphi] \Delta T \\ \dot{\Delta h} = -\omega_0 \Delta T \end{cases} \tag{B1}$$

Initial conditions for (B1) are

$$\begin{cases} \Delta T(t_1) = F_0 \Delta t \cdot \left[1 + \frac{1}{2} R(t_0) \Delta t\right] \\ \Delta h(t_1) = -F_0 \omega_0 \Delta t^2 \cdot \left[\frac{1}{2} + \frac{1}{6} R(t_0) \Delta t\right] \end{cases} \tag{B2}$$

which are the values of the instantaneous solution.

Considering a weakly dissipative system, where R_1 is small, ΔT and Δh can be expanded in powers of the small parameter R_1:

$$\Delta T = \Delta T_0 + R_1 \Delta T_1 + R_1^2 \Delta T_2 \ldots, \quad \Delta h = \Delta h_0 + R_1 \Delta h_1 + R_1^2 \Delta h_2 \ldots$$

Substituting these expansions into the governing equations yields the zeroth-order and first-order systems, respectively.

$$\begin{cases} \dot{\Delta T_0} = \omega_0 \Delta h_0 \\ \dot{\Delta h_0} = -\omega_0 \Delta T_0 \end{cases} \tag{B3}$$

$$\begin{cases} \dot{\Delta T_1} = \omega_0 \Delta h_1 - \sin\left(\omega_1 t_1 + \omega_1 t_2 + \varphi\right) \Delta T_0 \\ \dot{\Delta h_1} = -\omega_0 \Delta T_1 \end{cases} \tag{B4}$$

The general solution of the zeroth-order equation (B3) can be readily written as:

$$\begin{cases} \Delta T_0(t_2) = C_1 \cos(\omega_0 t_2) + C_2 \sin(\omega_0 t_2) = +R_c \cos(\omega_0 t_2 - \psi) \\ \Delta h_0(t_2) = C_2 \cos(\omega_0 t_2) - C_1 \sin(\omega_0 t_2) = -R_c \sin(\omega_0 t_2 - \psi) \end{cases} \tag{B5}$$

Here,

$$C_1 = F_0 \Delta t, \quad C_2 = -\frac{1}{2} F_0 \omega_0 \Delta t^2, \quad R_c = \sqrt{C_1^2 + C_2^2}, \quad \psi = \operatorname{atan2}(C_2, C_1)$$

1. Particular solution of the first-order system

Eliminating Δh_1 from Eq. (B4) yields:

$$\Delta T_1'' + \omega_0^2 \Delta T_1 = f(t_2) \tag{B6}$$

Here,

$$f(t_2) = -\frac{C_1}{2}[\Omega_2 \cos(\Omega_2 t_2 + \Omega_0) + \Omega_1 \cos(\Omega_1 t_2 + \Omega_0)] + \frac{C_2}{2}[\Omega_1 \sin(\Omega_1 t_2 + \Omega_0) - \Omega_2 \sin(\Omega_2 t_2 + \Omega_0)]$$

$$\Omega_0 = \omega_1 t_1 + \varphi, \;\; \Omega_1 = \omega_1 - \omega_0, \;\; \Omega_2 = \omega_1 + \omega_0$$

For each harmonic term $f_j(t) = A_j \sin(\Omega_j t + \varphi_j)$, the particular solution to $T'' + \omega_0^2 T = f_j(t)$ is:

$$T_{p,j}(t) = \frac{A_j}{\omega_0^2 - \Omega_j^2} \sin(\Omega_j t + \varphi_j), \quad j = 1,2,3,4 \tag{B7}$$

where, $\Omega_j \neq \omega_0$, subscript "p" denotes the particular solution.

According to Eq. (B7), four particular solutions can be obtained. Summing these contributions yields the particular solution for the first-order variables

$$\Delta T_{1,p}(t_2) = -\frac{B}{2}[C_1 \cos(\Omega_2 t_2 + \Omega_0) + C_2 \sin(\Omega_2 t_2 + \Omega_0)]$$

$$-\frac{A}{2}[C_1 \cos(\Omega_1 t_2 + \Omega_0) - C_2 \sin(\Omega_1 t_2 + \Omega_0)] \tag{B8}$$

where

$$A = \frac{\omega_1 - \omega_0}{\omega_0^2 - (\omega_1 - \omega_0)^2}, \quad B = \frac{\omega_1 + \omega_0}{\omega_0^2 - (\omega_1 + \omega_0)^2}$$

2. General solution of the first-order system

The complete first-order solution is given by the sum of the particular solution and the homogeneous solution of the system (B6), i.e.,

$$\Delta T_1(t_2) = \Delta T_{1,p}(t_2) + Q_1 \cos(\omega_0 t_2) + Q_2 \sin(\omega_0 t_2) \tag{B9}$$

When $t_2 = 0$, the initial value of ΔT_1 can be obtained from Eq. (B2):

$$\Delta T_1(0) = C_3, \quad \Delta T_1{}'(0) = \omega_0 C_4 - \sin(\Omega_0)\, C_1 \tag{B10}$$

where

$$C_3 = -\frac{1}{2} F_0 \Delta t^2 \, \sin(\omega_1 t_0 + \varphi), \quad C_4 = \frac{F_0 \omega_0 \Delta t^3}{6} \, \sin(\omega_1 t_0 + \varphi)$$

Substituting the initial condition (B10) into Eq. (B9) yields:

$$Q_1 = C_3 - \Delta T_{1,p}(0), \quad Q_2 = C_4 - \frac{\sin(\Omega_0) C_1 + \Delta T_{1,p}{}'(0)}{\omega_0}$$

Finally, the complete first-order solution is given by:

$$\Delta T_1(t_2) = \left[C_3 - \Delta T_{1,p}(0)\right]\cos(\omega_0 t_2) + \left[C_4 - \frac{\sin(\Omega_0) C_1 + \Delta T_{1,p}{}'(0)}{\omega_0}\right]\sin(\omega_0 t_2) + \Delta T_{1,p}(t_2)$$

$$= R_0 \cos(\omega_0 t_2 - \varphi_0) - \tfrac{1}{2} R_c [A \cos(\Omega_1 t_2 + \Omega_0 + \psi) + B \cos(\Omega_2 t_2 + \Omega_0 - \psi)] \tag{B11}$$

where

$$\Delta T_{1,p}(0) = -\frac{C_1}{2}(A + B)\cos\Omega_0 + \frac{C_2}{2}(A - B)\sin\Omega_0$$

$$\Delta T_{1,p}{}'(0) = \sin\Omega_0 \cdot \frac{C_1}{2}(A\Omega_1 + B\Omega_2) + \cos\Omega_0 \cdot \frac{C_2}{2}(A\Omega_1 - B\Omega_2)$$

$$R_0 = \sqrt{P^2 + Q^2}, \quad \varphi_0 = \mathrm{atan2}(Q, P)$$

$$P = C_3 + \frac{1}{2}[(A + B) C_1 \cos\Omega_0 - (A - B) C_2 \sin\Omega_0]$$

$$Q = C_4 - \left\{[1 + \frac{1}{2}(A\Omega_1 + B\Omega_2)] C_1 \sin\Omega_0 + \frac{1}{2}(A\Omega_1 - B\Omega_2) C_2 \cos\Omega_0\right\} / \omega_0$$

R_0 and φ_0 denote the same-frequency composite amplitude and phase of the adjustment term, respectively.

Equation (B11) can be further rewritten as a single sinusoidal (or cosine) form with ω_0 as the dominant frequency, whose amplitude and phase are modulated by the seasonal phase. To proceed, we first define:

$$\theta \equiv \omega_1 t_2 + \Omega_0, \quad x \equiv \omega_0 t_2 - \psi$$

Therefore,

$$\cos(\Omega_1 t_2 + \Omega_0 + \psi) = \cos(x - \theta), \quad \cos(\Omega_2 t_2 + \Omega_0 - \psi) = \cos(x + \theta)$$

Substituting these expressions back into Eq. (B11) and applying the sum–to–product trigonometric identities yields:

$$\Delta T_1(t_2) = R_0[\cos x \cos(\psi - \varphi_0) - \sin x \sin(\psi - \varphi_0)]$$

$$-\frac{1}{2} R_c[(A + B)\cos\theta \cos x + (A - B)\sin\theta \sin x]$$

$$= C(\theta)\cos x + S(\theta)\sin x = M(\theta)\cos(x - \gamma(\theta)) \tag{B12}$$

where

$$C(\theta) = R_0 \cos(\psi - \varphi_0) - \frac{A + B}{2} R_c \cos\theta$$

$$S(\theta) = -R_0 \sin(\psi - \varphi_0) - \frac{A - B}{2} R_c \sin\theta$$

$$M(\theta) = \sqrt{C(\theta)^2 + S(\theta)^2}, \quad \gamma(\theta) = \text{atan2}\big(S(\theta), C(\theta)\big)$$

Therefore, the first-order solution (B12) represents a single harmonic with the ENSO intrinsic phase $x = \omega_0 t_2 - \psi$ as the independent variable. Its amplitude $M(\theta)$ and phase shift $\gamma(\theta)$ are modulated only through the seasonal phase $\theta = \omega_1(t_1 + t_2) + \varphi$ and the constants $R_0, R_c, A, B, \psi, \varphi_0$.

3. Complete solution of the adjustment response

Finally, we obtain the solution to the adjustment-response system (B1). Neglecting the second-order terms $O(R_1^2)$, the solution can be written as the combination of the zeroth-order solution (B5) and the first-order solution (B12), yielding:

$$\Delta T(t_1 + t_2) \approx \Delta T_0(t_2) + R_1\,\Delta T_1(t_2)$$

$$= R_c\cos(\omega_0 t_2 - \psi) + R_1 M(\theta)\cos(\omega_0 t_2 - \psi - \gamma(\theta)) \quad \text{(B13)}$$

where R_c is constant, R_1 is small parameter and θ denotes the seasonal phase.

The zeroth-order term can be referred to as the free same-frequency response. Physically, it represents the "instantaneous impulse" imposed on the system by the WWB during the pulse interval Δt, which sets the initial perturbation state of the system (i.e., the instantaneous responses of temperature and thermocline depth anomalies derived in Appendix A). Thereafter, the system evolves freely at the intrinsic ENSO frequency ω_0, without direct coupling to the contemporaneous seasonal growth rate. Its amplitude R_c depends solely on the intensity and duration of the WWB and is independent of the season in which the WWB occurs.

The first-order term can be referred to as the seasonally modulated adjustment response. Mathematically, it is equivalent to a single harmonic with the intrinsic frequency ω_0, whose amplitude and phase vary slowly with the seasonal cycle. This can be interpreted as a simple oscillator with intrinsic frequency ω_0 coupled to a seasonally varying amplifier or damper. Physically, this term represents the delayed evolution of the system after a WWB event. The WWB excites Kelvin and Rossby waves that modify the thermocline slope and warm-water volume (the recharge–discharge process). Through the Bjerknes positive feedback, this perturbation subsequently undergoes delayed amplification or decay under the modulation of the seasonal growth rate $R(t)$. In this formulation, the amplitude $M(\theta)$ arises from the cumulative integral effect of the system's adjustment, while the phase shift $\gamma(\theta)$ originates from dynamical inertia. Both depend explicitly on the seasonal phase θ, thereby reflecting the sensitivity of the response to the timing of the WWB. In essence, the final SST response amplitude is determined by the temporal convolution between thermocline adjustment and the seasonal growth rate.

Using the same method, we can obtain

$$\Delta h(t_1 + t_2) \approx \Delta h_0(t_2) + R_1\Delta h_1(t_2)$$

$$= -R_c\sin(\omega_0 t_2 - \psi) - R_1 M_h(\theta)\sin\left(x - \gamma_h(\theta)\right) \quad \text{(B14)}$$

where

$$M_h(\theta) = \sqrt{C_h(\theta)^2 + S_h(\theta)^2}, \quad \gamma_h(\theta) = \text{atan2}(S_h(\theta), C_h(\theta))$$

$$C_h(\theta) = R_0 \cos(\psi - \varphi_0) - \frac{\omega_0 R_c}{2}\left(\frac{B}{\Omega_2} - \frac{A}{\Omega_1}\right)\cos\theta$$

$$S_h(\theta) = -R_0 \sin(\psi - \varphi_0) + \frac{\omega_0 R_c}{2}\left(\frac{B}{\Omega_2} + \frac{A}{\Omega_1}\right)\sin\theta$$

The solution for the adjustment response given by Eqs. (B13)–(B14) can be further simplified. If the characteristic time scale of the WWB influence is assumed to be small compared with the ENSO period (taken here as 4 years), i.e., $t_2 \ll 1/\omega_0$ (for example, t_2~3 months), then the trigonometric functions involving $\omega_0 t_2$ in the equations can be expanded in a Taylor series with respect to t_2:

$$\cos(\omega_0 t_2) = 1 + O(t_2), \quad \sin(\omega_0 t_2) = \omega_0 t_2 + O({t_2}^2) \tag{B15}$$

Substituting Eq. (B15) into Eqs. (B13)–(B14), and taking into account the cumulative effect of $R(t)$ over the interval t_2, we obtain after simplification:

$$\Delta T(t_1 + t_2) = C_1 + R_1 C_3 + \omega_0 C_2 t_2 + R_1(\omega_0 C_4 - \sin(\Omega_0) C_1) t_2$$

$$= \Delta T(t_1) - \frac{1}{2} F_0 (\omega_0 \Delta t)^2 \left[1 + \frac{1}{3} R(t_0)\Delta t - \frac{2}{(\omega_0 \Delta t)^2} R(t_1)\Delta t\right] t_2$$

$$\approx F_0 \Delta t \cdot \left[1 + \tfrac{1}{2} R(t_0)\Delta t + \int_{t_1}^{t_1+t_2} R(\tau) d\tau\right] \tag{B16}$$

$$\Delta h(t_1 + t_2) \approx -F_0 \omega_0 \Delta t \left\{\Delta t \left[\tfrac{1}{2} + \tfrac{1}{6} R(t_0)\Delta t\right] + t_2 \left[1 + \tfrac{1}{2} R(t_0)\Delta t + \tfrac{1}{2}\int_{t_1}^{t_1+t_2} R(\tau) d\tau\right]\right\} \tag{B17}$$

The phase of the adjustment response is determined by the time integral of $R(t)$ over the interval t_2. When $t_2 = 0$, Eqs. (B16)–(B17) reduce to (A16)–(A17).

824 REFERENCES

825 Alam, M. T., and Y. Tang, 2021: Impact of Westerly Wind Bursts on ENSO Based on a Hybrid
826 Coupled Model: Part I – ENSO Simulation. *Atmosphere-Ocean*, **59**, 233–245,
827 https://doi.org/10.1080/07055900.2021.1973362.

828 ——, ——, and S. Ul Islam, 2023: Impact of Westerly Wind Bursts (WWBs) on ENSO based on
829 a Hybrid Coupled Model: Part II – ENSO Prediction. *Atmosphere-Ocean*, **61**, 186–196,
830 https://doi.org/10.1080/07055900.2023.2173555.

831 An, S.-I., and F.-F. Jin, 2011: Linear solutions for the frequency and amplitude modulation of
832 ENSO by the annual cycle. *Tellus Dyn. Meteorol. Oceanogr.*, **63**, 238,
833 https://doi.org/10.1111/j.1600-0870.2010.00482.x.

834 Chen, D., and Coauthors, 2015: Strong influence of westerly wind bursts on El Niño diversity.
835 *Nat. Geosci.*, **8**, 339–345, https://doi.org/10.1038/ngeo2399.

836 Chen, H., and F. Jin, 2022: Dynamics of ENSO Phase–Locking and Its Biases in Climate Models.
837 *Geophys. Res. Lett.*, **49**, e2021GL097603, https://doi.org/10.1029/2021GL097603.

838 Chen, H.-C., and F.-F. Jin, 2020: Fundamental Behavior of ENSO Phase Locking. *J. Clim.*, **33**,
839 1953–1968, https://doi.org/10.1175/JCLI-D-19-0264.1.

840 ——, and ——, 2023: The mechanism of boreal summer SSTA phase-locking in the far eastern
841 Pacific. *Npj Clim. Atmospheric Sci.*, **6**, 138, https://doi.org/10.1038/s41612-023-00472-6.

842 Chiodi, A. M., and D. E. Harrison, 2017: Observed El Niño SSTA development and the effects of
843 easterly and westerly wind events in 2014/15. *J. Clim.*, **30**, 1505–1519.

844 Drushka, K., H. Bellenger, E. Guilyardi, M. Lengaigne, J. Vialard, and G. Madec, 2015: Processes
845 driving intraseasonal displacements of the eastern edge of the warm pool: the contribution
846 of westerly wind events. *Clim. Dyn.*, **44**, 735–755, https://doi.org/10.1007/s00382-014-
847 2297-z.

848 Ehsan, M. A., M. L. L'Heureux, M. K. Tippett, A. W. Robertson, and J. Turmelle, 2024: Real-
849 time ENSO forecast skill evaluated over the last two decades, with focus on the onset of
850 ENSO events. *Npj Clim. Atmospheric Sci.*, **7**, 301, https://doi.org/10.1038/s41612-024-
851 00845-5.

852 Eisenman, I., L. Yu, and E. Tziperman, 2005: Westerly Wind Bursts: ENSO's Tail Rather than the
853 Dog?, https://doi.org/10.1175/JCLI3588.1.

854 Fedorov, A. V., and S. Hu, 2016: The development of extreme El Niño in 2015: the role of
855 westerly and easterly wind bursts, and preconditioning by the failed 2014 event. *AGU Fall*
856 *Meeting Abstracts*, Vol. 2016 of, A34E-07.

857 Fedorov, A. V., S. Hu, M. Lengaigne, and E. Guilyardi, 2015: The impact of westerly wind bursts
858 and ocean initial state on the development, and diversity of El Niño events. *Clim. Dyn.*, **44**,
859 1381–1401, https://doi.org/10.1007/s00382-014-2126-4.

860 Galanti, E., and E. Tziperman, 2000: ENSO's phase locking to the seasonal cycle in the fast-SST,
861 fast-wave, and mixed-mode regimes. *J. Atmospheric Sci.*, **57**, 2936–2950.

Gebbie, G., I. Eisenman, A. Wittenberg, and E. Tziperman, 2007: Modulation of Westerly Wind Bursts by Sea Surface Temperature: A Semistochastic Feedback for ENSO. *J. Atmospheric Sci.*, **64**, 3281–3295, https://doi.org/10.1175/JAS4029.1.

Ham, Y. G., J. H. Kim, and J. J. Luo, 2019: Deep learning for multi-year ENSO forecasts. *Nature*, **573**, 568–572, https://doi.org/10.1038/s41586-019-1559-7.

Harrison, D. E., and B. S. Giese, 1991: Episodes of surface westerly winds as observed from islands in the western tropical Pacific. *J. Geophys. Res. Oceans*, **96**, 3221–3237, https://doi.org/10.1029/90JC01775.

——, and G. A. Vecchi, 1997: Westerly Wind Events in the Tropical Pacific, 1986–95.

Heaney, A. K., J. Shaman, and K. A. Alexander, 2019: El Niño-Southern oscillation and under-5 diarrhea in Botswana. *Nat. Commun.*, **10**, 5798.

Henson, C., P. Market, A. Lupo, and P. Guinan, 2017: ENSO and PDO-related climate variability impacts on Midwestern United States crop yields. *Int. J. Biometeorol.*, **61**, 857–867, https://doi.org/10.1007/s00484-016-1263-3.

Hersbach, H., and Coauthors, 2020: The ERA5 global reanalysis. *Q. J. R. Meteorol. Soc.*, **146**, 1999–2049, https://doi.org/10.1002/qj.3803.

Hsiang, S. M., K. C. Meng, and M. A. Cane, 2011: Civil conflicts are associated with the global climate. *Nature*, **476**, 438–441.

Hu, J., B. Weng, T. Huang, J. Gao, F. Ye, and L. You, 2021: Deep Residual Convolutional Neural Network Combining Dropout and Transfer Learning for ENSO Forecasting. *Geophys. Res. Lett.*, **48**, e2021GL093531, https://doi.org/10.1029/2021GL093531.

Hu, S., and A. V. Fedorov, 2016: Exceptionally strong easterly wind burst stalling El Niño of 2014. *Proc. Natl. Acad. Sci.*, **113**, 2005–2010, https://doi.org/10.1073/pnas.1514182113.

——, and ——, 2019: The extreme El Niño of 2015–2016: the role of westerly and easterly wind bursts, and preconditioning by the failed 2014 event. *Clim. Dyn.*, **52**, 7339–7357, https://doi.org/10.1007/s00382-017-3531-2.

Huang, B., C. Liu, V. Banzon, E. Freeman, G. Graham, B. Hankins, T. Smith, and H.-M. Zhang, 2021: Improvements of the daily optimum interpolation sea surface temperature (DOISST) version 2.1. *J. Clim.*, **34**, 2923–2939.

——, and Coauthors, 2025: Extended Reconstructed Sea Surface Temperature, Version 6 (ERSSTv6). Part I: An Artificial Neural Network Approach, https://doi.org/10.1175/JCLI-D-23-0707.1.

Ji, C., M. Mu, X. Fang, and L. Tao, 2023: Improving the forecasting of El Niño amplitude based on an ensemble forecast strategy for westerly wind bursts. *J. Clim.*, **36**, 8675–8694.

Jin, E. K., and Coauthors, 2008: Current status of ENSO prediction skill in coupled ocean–atmosphere models. *Clim. Dyn.*, **31**, 647–664, https://doi.org/10.1007/s00382-008-0397-3.

Jin, F.-F., 1997: An Equatorial Ocean Recharge Paradigm for ENSO. Part I: Conceptual Model. *J. Atmospheric Sci.*, **54**, 811–829, https://doi.org/10.1175/1520-0469(1997)054%253C0811:AEORPF%253E2.0.CO;2.

Jin, Y., and Z. Liu, 2021: A Theory of the Spring Persistence Barrier on ENSO. Part I: The Role of ENSO Period. *J. Clim.*, **34**, 2145–2155, https://doi.org/10.1175/jcli-d-20-0540.1.

——, ——, Z. Lu, and C. He, 2019: Seasonal Cycle of Background in the Tropical Pacific as a Cause of ENSO Spring Persistence Barrier. *Geophys. Res. Lett.*, **46**, 13371–13378, https://doi.org/10.1029/2019GL085205.

Lehodey, P., and Coauthors, 2020: ENSO Impact on Marine Fisheries and Ecosystems. *Geophysical Monograph Series*, M.J. McPhaden, A. Santoso, and W. Cai, Eds., Wiley, 429–451, https://doi.org/10.1002/9781119548164.ch19.

Lengaigne, M., J. Boulanger, C. Menkes, S. Masson, G. Madec, and P. Delecluse, 2002: Ocean response to the March 1997 Westerly Wind Event. *J. Geophys. Res. Oceans*, **107**, https://doi.org/10.1029/2001JC000841.

——, E. Guilyardi, J.-P. Boulanger, C. Menkes, P. Delecluse, P. Inness, J. Cole, and J. Slingo, 2004: Triggering of El Niño by westerly wind events in a coupled general circulation model. *Clim. Dyn.*, **23**, 601–620, https://doi.org/10.1007/s00382-004-0457-2.

Levine, A. F. Z., and M. J. McPhaden, 2015: The annual cycle in ENSO growth rate as a cause of the spring predictability barrier. *Geophys. Res. Lett.*, **42**, 5034–5041, https://doi.org/10.1002/2015GL064309.

Lian, T., and D. Chen, 2021: The essential role of early-spring westerly wind bursts in generating the centennial extreme 1997/98 El Niño. *J. Clim.*, **34**, 8377–8388.

Liao, H., C. Wang, and Z. Song, 2021: ENSO phase-locking biases from the CMIP5 to CMIP6 models and a possible explanation. *Deep Sea Res. Part II Top. Stud. Oceanogr.*, **189–190**, 104943, https://doi.org/10.1016/j.dsr2.2021.104943.

Liu, Y., W. Zhang, F. Jiang, H. Chen, F. Jin, and S. Hu, 2025: Diverse Timing of El Niño Onset Linked to Preconditioned Recharge State and Occurrence of Westerly Wind Bursts. *Geophys. Res. Lett.*, **52**, e2024GL113668, https://doi.org/10.1029/2024GL113668.

Liu, Z., Y. Jin, and X. Rong, 2019: A theory for the seasonal predictability barrier: Threshold, timing, and intensity. *J. Clim.*, **32**, 423–443, https://doi.org/10.1175/JCLI-D-18-0383.1.

Luo, J.-J., S. Masson, S. K. Behera, and T. Yamagata, 2008: Extended ENSO Predictions Using a Fully Coupled Ocean–Atmosphere Model. *J. Clim.*, **21**, 84–93, https://doi.org/10.1175/2007jcli1412.1.

McPhaden, M. J., 2003: Tropical Pacific Ocean heat content variations and ENSO persistence barriers. *Geophys. Res. Lett.*, **30**, 2003GL016872, https://doi.org/10.1029/2003GL016872.

——, and X. Yu, 1999: Equatorial waves and the 1997–98 El Niño. *Geophys. Res. Lett.*, **26**, 2961–2964, https://doi.org/10.1029/1999GL004901.

——, H. P. Freitag, S. P. Hayes, B. A. Taft, Z. Chen, and K. Wyrtki, 1988: The response of the equatorial Pacific Ocean to a westerly wind burst in May 1986. *J. Geophys. Res. Oceans*, **93**, 10589–10603, https://doi.org/10.1029/JC093iC09p10589.

——, A. Santoso, and W. Cai, eds., 2020: *El Niño Southern Oscillation in a Changing Climate*. 1st ed. Wiley, https://doi.org/10.1002/9781119548164.

Meinen, C. S., and M. J. McPhaden, 2000: Observations of warm water volume changes in the equatorial Pacific and their relationship to El Niño and La Niña. *J. Clim.*, **13**, 3551–3559.

Menkes, C. E., M. Lengaigne, J. Vialard, M. Puy, P. Marchesiello, S. Cravatte, and G. Cambon, 2014: About the role of Westerly Wind Events in the possible development of an El Niño in 2014. *Geophys. Res. Lett.*, **41**, 6476–6483, https://doi.org/10.1002/2014GL061186.

Moore, A. M., and R. Kleeman, 1996: The dynamics of error growth and predictability in a coupled model of ENSO. *Q. J. R. Meteorol. Soc.*, **122**, 1405–1446, https://doi.org/10.1002/qj.49712253409.

Petrova, D., J. Ballester, S. J. Koopman, and X. Rodó, 2020: Multiyear statistical prediction of ENSO enhanced by the tropical Pacific observing system. *J. Clim.*, **33**, 163–174, https://doi.org/10.1175/JCLI-D-18-0877.1.

Puy, M., J. Vialard, M. Lengaigne, and E. Guilyardi, 2015: Modulation of equatorial Pacific westerly/easterly wind events by the Madden–Julian oscillation and convectively-coupled Rossby waves. *Clim. Dyn.*, **46**, 2155–2178, https://doi.org/10.1007/s00382-015-2695-x.

——, J. Vialard, M. Lengaigne, E. Guilyardi, A. Voldoire, and G. Madec, 2016: Modulation of equatorial Pacific sea surface temperature response to westerly wind events by the oceanic background state. *Clim. Dyn.*, **52**, 7267–7291, https://doi.org/10.1007/s00382-016-3480-1.

——, and Coauthors, 2019: Influence of Westerly Wind Events stochasticity on El Niño amplitude: the case of 2014 vs. 2015. *Clim. Dyn.*, **52**, 7435–7454, https://doi.org/10.1007/s00382-017-3938-9.

Rayner, N. A., D. E. Parker, E. B. Horton, C. K. Folland, L. V. Alexander, D. P. Rowell, E. C. Kent, and A. Kaplan, 2003: Global analyses of sea surface temperature, sea ice, and night marine air temperature since the late nineteenth century. *J. Geophys. Res. Atmospheres*, **108**, 2002JD002670, https://doi.org/10.1029/2002JD002670.

Ren, H., F. Jin, B. Tian, and A. A. Scaife, 2016: Distinct persistence barriers in two types of ENSO. *Geophys. Res. Lett.*, **43**, https://doi.org/10.1002/2016GL071015.

Ren, H.-L., J. Zuo, and Y. Deng, 2018: Statistical predictability of Niño indices for two types of ENSO. *Clim. Dyn.*, **52**, 5361–5382, https://doi.org/10.1007/s00382-018-4453-3.

——, and Coauthors, 2019: Seasonal predictability of winter ENSO types in operational dynamical model predictions. *Clim. Dyn.*, **52**, 3869–3890, https://doi.org/10.1007/s00382-018-4366-1.

Saha, S., and Coauthors, 2014: The NCEP climate forecast system version 2. *J. Clim.*, **27**, 2185–2208.

Santoso, A., and Coauthors, 2019: Dynamics and predictability of El Niño–Southern Oscillation: An Australian perspective on progress and challenges. *Bull. Am. Meteorol. Soc.*, **100**, 403–420.

Seiki, A., and Y. N. Takayabu, 2007: Westerly wind bursts and their relationship with intraseasonal variations and ENSO. Part I: Statistics. *Mon. Weather Rev.*, **135**, 3325–3345.

Stein, K., N. Schneider, A. Timmermann, and F.-F. Jin, 2010: Seasonal Synchronization of ENSO Events in a Linear Stochastic Model*. *J. Clim.*, **23**, 5629–5643, https://doi.org/10.1175/2010JCLI3292.1.

——, A. Timmermann, N. Schneider, F.-F. Jin, and M. F. Stuecker, 2014: ENSO Seasonal Synchronization Theory.

Tan, X., Y. Tang, T. Lian, S. Zhang, T. Liu, and D. Chen, 2020: Effects of Semistochastic Westerly Wind Bursts on ENSO Predictability. *Geophys. Res. Lett.*, **47**, e2019GL086828, https://doi.org/10.1029/2019GL086828.

Thompson, C. J., and D. S. Battisti, 2001: A Linear Stochastic Dynamical Model of ENSO. Part II: Analysis. *J. Clim.*, **14**, 445–466, https://doi.org/10.1175/1520-0442(2001)014%253C0445:ALSDMO%253E2.0.CO;2.

Tziperman, E., M. A. Cane, and S. E. Zebiak, 1995: Irregularity and locking to the seasonal cycle in an ENSO prediction model as explained by the quasi-periodicity route to chaos. *J. Atmospheric Sci.*, **52**, 293–306, https://doi.org/10.1175/1520-0469(1995)052%253C0293:IALTTS%253E2.0.CO;2.

——, S. E. Zebiak, and M. A. Cane, 1997: Mechanisms of Seasonal – ENSO Interaction. *J. Atmospheric Sci.*, **54**, 61–71, https://doi.org/10.1175/1520-0469(1997)054%253C0061:MOSEI%253E2.0.CO;2.

Wang, X., J. Slawinska, and D. Giannakis, 2020: Extended-range statistical ENSO prediction through operator-theoretic techniques for nonlinear dynamics. *Sci. Rep.*, **10**, 2636.

Webster, P. J., and S. Yang, 1992: Monsoon and Enso: Selectively Interactive Systems. *Q. J. R. Meteorol. Soc.*, **118**, 877–926, https://doi.org/10.1002/qj.49711850705.

Wright, P. B., 1979: Persistence of rainfall anomalies in the central Pacific. *Nature*, **277**, 371–374, https://doi.org/10.1038/277371a0.

Yang, S., Z. Li, J.-Y. Yu, X. Hu, W. Dong, and S. He, 2018: El Niño–Southern Oscillation and its impact in the changing climate. *Natl. Sci. Rev.*, **5**, 840–857.

Yang, X., Y. Bao, Z. Song, Q. Shu, Y. Song, X. Wang, and F. Qiao, 2023: Key to ENSO phase-locking simulation: effects of sea surface temperature diurnal amplitude. *Npj Clim. Atmospheric Sci.*, **6**, 159, https://doi.org/10.1038/s41612-023-00483-3.

Yu, S., and A. V. Fedorov, 2020: The Role of Westerly Wind Bursts During Different Seasons Versus Ocean Heat Recharge in the Development of Extreme El Niño in Climate Models. *Geophys. Res. Lett.*, **47**, e2020GL088381, https://doi.org/10.1029/2020GL088381.

——, and ——, 2022: The essential role of westerly wind bursts in ENSO dynamics and extreme events quantified in model “wind stress shaving” experiments. *J. Clim.*, **35**, 7519–7538.

Zebiak, S. E., and M. A. Cane, 1987: A model El Niño–southern oscillation. *Mon. Weather Rev.*, **115**, 2262–2278.

Zhang, S., H. Wang, H. Jiang, and W. Ma, 2021: Evaluation of ENSO Prediction Skill Changes since 2000 Based on Multimodel Hindcasts. *Atmosphere*, **12**, 365, https://doi.org/10.3390/atmos12030365.

1017 Zheng, F., and J. Zhu, 2010: Spring predictability barrier of ENSO events from the perspective of
1018 an ensemble prediction system. *Glob. Planet. Change*, **72**, 108–117.

1019 Zheng, Y., M. Rugenstein, P. Pieper, G. Beobide-Arsuaga, and J. Baehr, 2022: El Niño–Southern
1020 Oscillation (ENSO) predictability in equilibrated warmer climates. *Earth Syst. Dyn.*, **13**,
1021 1611–1623.

1022